
Energy-based Hopfield Boosting for Out-of-Distribution Detection

Claus Hofmann^{1,2} Simon Schmid³ Bernhard Lehner^{2,4} Daniel Klotz⁵ Sepp Hochreiter^{1,2}

Abstract

Out-of-distribution (OOD) detection is critical when deploying machine learning models in the real world. Outlier exposure (OE) methods, which incorporate auxiliary outlier data (AUX) in the training process, can drastically improve OOD detection performance. We introduce Hopfield Boosting, a boosting approach, which leverages modern Hopfield energy to sharpen the decision boundary between the in-distribution (ID) and OOD data. Hopfield Boosting encourages the model to focus on hard-to-distinguish auxiliary outlier examples that lie close to the decision boundary between ID and AUX data. Our method achieves a new state-of-the-art in OOD detection with OE, improving the FPR95 from 2.28 to 0.92 on CIFAR-10, from 11.24 to 7.94 on CIFAR-100, and from 50.74 to 36.60 on ImageNet-1K.

1. Introduction

Out-of-distribution (OOD) detection is crucial when using machine learning systems in the real world (Ruff et al., 2021). Deployed models will — sooner or later — encounter inputs that deviate from the training distribution. For example, a system trained to recognize music genres might also hear a sound clip of construction site noise. In the best case, a naive deployment can then result in overly confident predictions. In the worst case, we will get erratic model behavior and completely wrong predictions (Hendrycks & Gimpel, 2017). The purpose of OOD detection is to classify these inputs as OOD, such that the system can then, for instance, notify users that no prediction is possible. In

*Equal contribution ¹Johannes Kepler University Linz, Institute for Machine Learning, JKU LIT SAL eSPML Lab, Austria ²Silicon Austria Labs, JKU LIT SAL eSPML Lab, Austria ³Software Competence Center Hagenberg GmbH, Austria ⁴Johannes Kepler University Linz, JKU LIT SAL eSPML Lab, Austria ⁵Department of Computational Hydrosystems, Helmholtz Centre for Environmental Research–UFZ, Leipzig, Germany. Correspondence to: Claus Hofmann <hofmann@ml.jku.at>.

Published at the 2nd Differentiable Almost Everything Workshop at the 41st International Conference on Machine Learning, Vienna, Austria. July 2024. Copyright 2024 by the author(s).

summary, our contributions are as follows:

1. We propose Hopfield Boosting, an OOD detection approach that samples weak learners by using the modern Hopfield energy (MHE; Ramsauer et al., 2021).
2. Hopfield Boosting achieves a new state-of-the-art in OOD detection. It improves the average false positive rate at 95% true positives (FPR95) from 2.28 to 0.92 on CIFAR-10, from 11.24 to 7.94 on CIFAR-100, and from 50.74 to 36.60 on ImageNet-1K.

2. Related Work

Post-hoc OOD detection. A common OOD detection approach is to use a post-hoc strategy, where one employs statistics obtained from a classifier. The perhaps most well-known approach in this class is the Maximum Softmax Probability (MSP; Hendrycks & Gimpel, 2017), where one utilizes $\max_y p(y | \mathbf{x})$ to estimate whether a sample is OOD. Despite good empirical performance, this view is intrinsically limited, since OOD detection should focus on $p(\mathbf{x})$. A wide range of post-hoc OOD detection approaches have been proposed to address the shortcomings of MSP (e.g., Liu et al., 2020; Sun et al., 2021; Djuricic et al., 2023). Most related to Hopfield Boosting is the work of Zhang et al. (2023a) – to our knowledge, they are the first to apply MHE to do OOD detection.

Auxiliary outlier data and outlier exposure. A second group of OOD detection approaches are outlier exposure (OE) methods. Like Hopfield Boosting, they incorporate AUX data in the training process to improve the detection of OOD samples (e.g., Hendrycks et al., 2019b; Liu et al., 2020; Ming et al., 2022). We provide more detailed discussions on a range of OE methods in Appendix C.1. As far as we know, all OE approaches optimize an objective (\mathcal{L}_{OOD}), which aims at improving the model’s discriminative power between in-distribution (ID) and OOD data using the AUX data set as a stand-in for the OOD case. In general, OE methods conceptualize the AUX data set as a large and diverse data set (e.g., ImageNet for vision tasks). Recent approaches therefore actively try to find informative samples close to the decision boundary between ID and AUX data for the training. The aim is to refine the decision boundary,

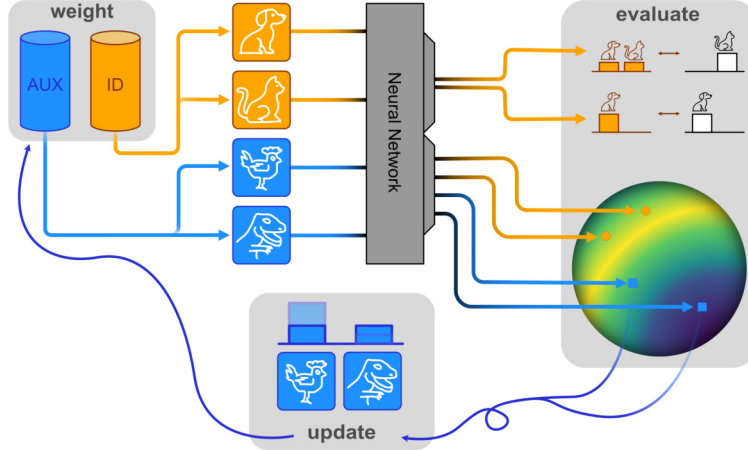


Figure 1: The Hopfield Boosting concept. The first step (weight) creates weak learners by firstly choosing in-distribution samples (ID, orange), and by secondly choosing auxiliary outlier samples (AUX, blue) according to their assigned probabilities; the second step (evaluate) computes the losses for the resulting predictions (Section 3); and the third step (update) assigns new probabilities to the AUX samples according to their position on the hypersphere (see Figure 2).

ensuring the ID data is more tightly encapsulated (e.g., [Ming et al., 2022](#)). Hopfield Boosting also makes use of samples close to the boundary by giving them higher weights for the boosting step.

Continuous modern Hopfield networks. MHNs are energy-based associative memory networks. They advance conventional Hopfield networks ([Hopfield, 1984](#)) by introducing continuous queries and states with the MHE as a new energy function. MHE leads to exponential storage capacity, while retrieval is possible with a one-step update ([Ramsauer et al., 2021](#)). Section 3.2 gives an introduction to MHE for OOD detection. For further details on MHNs, we refer to Appendix A.

3. Method

This section presents Hopfield Boosting: First, we formalize the OOD detection task. Second, we give an overview of the MHE. Finally, we introduce the boosting framework. Figure 1 shows a summary of Hopfield Boosting.

3.1. Classification and OOD Detection

Consider a multi-class classification task denoted as $(\mathbf{X}^D, \mathbf{Y}^D, \mathcal{Y})$, where $\mathbf{X}^D \in \mathbb{R}^{D \times N}$ represents a set of N D -dimensional feature vectors $(\mathbf{x}_1^D, \mathbf{x}_2^D, \dots, \mathbf{x}_N^D)$, which are i.i.d. samples $\mathbf{x}_i^D \sim p_{\text{ID}}$. $\mathbf{Y}^D \in \mathcal{Y}^N$ denotes the labels associated with these feature vectors, and \mathcal{Y} is a set containing possible classes. We consider an observation $\xi^D \in \mathbb{R}^D$ that deviates considerably from the data generation $p_{\text{ID}}(\xi^D)$ that defines the “normality” of our data as OOD. Following

[Ruff et al. \(2021\)](#), an observation is OOD if it is in the set

$$\mathbb{O} = \{\xi^D \in \mathbb{R}^D \mid p_{\text{ID}}(\xi^D) < \epsilon\} \text{ where } \epsilon > 0. \quad (1)$$

Since the probability density p_{ID} is in general not known, one needs to estimate $p_{\text{ID}}(\xi^D)$. In practice, it is common to define an outlier score $s(\xi)$ that uses a threshold γ and an encoder ϕ , where $\xi = \phi(\xi^D)$. The outlier score should — in the best case — preserve the density ranking. Given $s(\xi)$ and ϕ , OOD detection can be formulated as a binary classification task with the classes ID and OOD:

$$\hat{B}(\xi^D, \gamma) = \begin{cases} \text{ID} & \text{if } s(\phi(\xi^D)) \geq \gamma \\ \text{OOD} & \text{if } s(\phi(\xi^D)) < \gamma \end{cases}. \quad (2)$$

3.2. Modern Hopfield Energy

The log-sum-exponential (lse) function is defined as

$$\text{lse}(\beta, \mathbf{z}) = \beta^{-1} \log \left(\sum_{i=1}^N \exp(\beta z_i) \right), \quad (3)$$

where β is the inverse temperature and $\mathbf{z} \in \mathbb{R}^N$ is a vector. The lse can be seen as a soft approximation to the maximum function: As $\beta \rightarrow \infty$, the lse approaches $\max_i z_i$.

Given a set of N d -dimensional stored patterns $(\mathbf{x}_1, \mathbf{x}_2, \dots, \mathbf{x}_N)$ arranged in a data matrix \mathbf{X} , and a d -dimensional query ξ , the MHE is defined as

$$E(\xi; \mathbf{X}) = -\text{lse}(\beta, \mathbf{X}^T \xi) + \frac{1}{2} \xi^T \xi + C, \quad (4)$$

where $C = \beta^{-1} \log N + \frac{1}{2} M^2$ and M is the largest norm of a pattern: $M = \max_i \|\mathbf{x}_i\|$. \mathbf{X} is also called the memory of the MHN.

To use the MHE for OOD detection, Hopfield Boosting acquires the memory patterns \mathbf{X} by feeding raw data instances $(\mathbf{x}_1^{\mathcal{D}}, \mathbf{x}_2^{\mathcal{D}}, \dots, \mathbf{x}_N^{\mathcal{D}})$ of the ID data set arranged in the data matrix $\mathbf{X}^{\mathcal{D}} \in \mathbb{R}^{D \times N}$ to an encoder $\phi : \mathbb{R}^D \rightarrow \mathbb{R}^d$ (e.g., ResNet): $\mathbf{x}_i = \phi(\mathbf{x}_i^{\mathcal{D}})$. We denote the component-wise application of ϕ to the patterns in $\mathbf{X}^{\mathcal{D}}$ as $\mathbf{X} = \phi(\mathbf{X}^{\mathcal{D}})$. Similarly, a raw query $\xi^{\mathcal{D}} \in \mathbb{R}^D$ is fed through the encoder to obtain the query pattern: $\xi = \phi(\xi^{\mathcal{D}})$. One can now use $E(\xi; \mathbf{X})$ to estimate whether ξ is ID or OOD: A low energy indicates ξ is ID, and a high energy signifies that ξ is OOD. The MHE can be viewed as a soft, continuously differentiable approximation to the nearest neighbor similarity: As $\beta \rightarrow \infty$, the lse term in the MHE returns the dot-product similarity of ξ to its nearest neighbor in \mathbf{X} .

3.3. Boosting Framework

Sampling of informative outlier data. Similar to [Ming et al. \(2022\)](#), Hopfield Boosting selects informative outliers close to the ID-OOD decision boundary. For this selection, Hopfield Boosting constructs a distribution over the AUX data similar to AdaBoost ([Freund & Schapire, 1995](#)) by sampling data instances close to the decision boundary more frequently. We refer to samples close to the decision boundary as weak learners — their nearest neighbors consist of samples from their own class as well as from the foreign class. The Hopfield Boosting mechanism thus results in the special setup where a (projected) data point becomes a weak learner itself. That is, it is possible to use this data point to construct a classifier that barely performs better than random guessing (see [Appendix E.5](#)). Vice versa, a strong hypothesis can be created by forming an ensemble of a set of weak learners ([Figure 2](#)).

We denote the matrix with the raw AUX data instances $(\mathbf{o}_1^{\mathcal{D}}, \dots, \mathbf{o}_N^{\mathcal{D}})$ as $\mathbf{O}^{\mathcal{D}} \in \mathbb{R}^{D \times M}$, and the memory containing the encoded AUX patterns as $\mathbf{O} = \phi(\mathbf{O}^{\mathcal{D}})$. The boosting proceeds as follows: There exists a weight (w_1, \dots, w_M) for each data point in $\mathbf{O}^{\mathcal{D}}$. The individual weights are aggregated into the weight vector \mathbf{w}_t . Hopfield Boosting uses these weights to draw mini-batches $\mathbf{O}_s^{\mathcal{D}}$ from $\mathbf{O}^{\mathcal{D}}$ for training, where weak learners receive higher weights.

We introduce an MHE-based energy function which Hopfield Boosting uses to determine how weak a specific learner ξ is (with higher energy indicating a weaker learner).

$$E_b(\xi; \mathbf{X}, \mathbf{O}) = -2 \operatorname{lse}(\beta, (\mathbf{X} \parallel \mathbf{O})^T \xi) + \operatorname{lse}(\beta, \mathbf{X}^T \xi) + \operatorname{lse}(\beta, \mathbf{O}^T \xi), \quad (5)$$

where $(\mathbf{X} \parallel \mathbf{O}) \in \mathbb{R}^{d \times (N+M)}$ denotes the concatenated data matrix containing the patterns from both \mathbf{X} and \mathbf{O} . Before computing E_b , we normalize the feature vectors in \mathbf{X} , \mathbf{O} , and ξ to unit length. [Figure 3](#) displays the energy landscape of $E_b(\xi; \mathbf{X}, \mathbf{O})$ using exemplary data on a 3-dimensional sphere. E_b is maximal at the decision boundary between

ID and AUX data and decreases with increasing distance from the decision boundary in both directions. We provide a theoretical background on E_b in [Appendix F](#).

To calculate the weights \mathbf{w}_{t+1} , we use a collection of AUX patterns as a query matrix Ξ and compute the respective energies E_b of those patterns. The resulting energy vector $E_b(\Xi; \mathbf{X}, \mathbf{O})$ is then normalized by a softmax. This computation provides the updated weights:

$$\mathbf{w}_{t+1} = \operatorname{softmax}(\beta E_b(\Xi; \mathbf{X}, \mathbf{O})). \quad (6)$$

Training the model using MHE. In this section, we introduce how Hopfield Boosting uses the sampled weak learners to improve the detection of patterns outside the training distribution. We follow the established training method for OE (e.g., [Hendrycks et al., 2019b](#)): Train a classifier on the ID data using cross-entropy and add an OOD loss that uses the AUX data set to sharpen the decision boundary between the ID and OOD regions. This yields a composite loss

$$\mathcal{L} = \mathcal{L}_{\text{CE}} + \lambda \mathcal{L}_{\text{OOD}}, \quad (7)$$

Hopfield Boosting explicitly minimizes E_b . Given the weight vector \mathbf{w}_t , and the data sets $\mathbf{X}^{\mathcal{D}}$ and $\mathbf{O}^{\mathcal{D}}$, we obtain a mini-batch $\mathbf{X}_s^{\mathcal{D}}$ containing N_s samples from $\mathbf{X}^{\mathcal{D}}$ by uniform sampling, and a mini-batch of N_s weak learners $\mathbf{O}_s^{\mathcal{D}}$ from $\mathbf{O}^{\mathcal{D}}$ by sampling according to \mathbf{w}_t with replacement. We then feed the respective mini-batches into the neural network ϕ (e.g., ResNet) to create an embedding.

Hopfield Boosting computes \mathcal{L}_{OOD} as follows:

$$\mathcal{L}_{\text{OOD}} = \frac{1}{2N_s} \sum_{\xi} E_b(\xi; \mathbf{X}_s, \mathbf{O}_s), \quad (8)$$

where the memories \mathbf{X}_s and \mathbf{O}_s contain the embeddings of the sampled data instances: $\mathbf{X}_s = \phi(\mathbf{X}_s^{\mathcal{D}})$ and $\mathbf{O}_s = \phi(\mathbf{O}_s^{\mathcal{D}})$. The sum is taken over the observations ξ , which are drawn from $(\mathbf{X}_s \parallel \mathbf{O}_s)$. Hopfield Boosting computes \mathcal{L}_{OOD} for each mini-batch individually. To the best of our knowledge, Hopfield Boosting is the first method that uses Hopfield networks in this way to train a deep neural network. We note that there is a relation between Hopfield Boosting and SVMs with an RBF kernel (see [Appendix G.3](#)). However, the optimization procedure of SVMs is in general not differentiable. In contrast, our novel energy function is fully differentiable. This allows us to use it to train neural networks. [Rätsch et al. \(2001\)](#) shows the relation between highly weighted samples in AdaBoost and support vectors.

Inference. At inference time, the OOD score $s(\xi)$ is

$$s(\xi) = \operatorname{lse}(\beta, \mathbf{X}^T \xi) - \operatorname{lse}(\beta, \mathbf{O}^T \xi). \quad (9)$$

For computing $s(\xi)$, Hopfield Boosting uses the 50,000 random samples from the ID and AUX data sets, respectively.

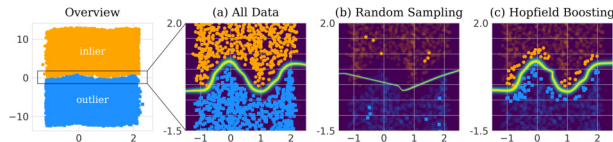


Figure 2: Synthetic example of the adaptive resampling mechanism. Hopfield Boosting forms a strong hypothesis by sampling and combining a set of weak hypotheses close to the decision boundary. The heatmap on the background shows $\exp(\beta E_b(\xi, \mathbf{X}, \mathbf{O}))$, where β is 60. Only the sampled (i.e., highlighted) points serve as memories \mathbf{X} and \mathbf{O} .

4. Experiments

This section first presents a toy example to give the reader an intuition of Hopfield Boosting, and then describes our experiments and results on CIFAR-10. For the selection of the hyperparameters and additional experiments, including ablations, additional baselines, and results on CIFAR-100 and ImageNet-1K, we refer to Appendix H.

4.1. Toy Example

Figure 2 demonstrates how the weighting in Hopfield Boosting allows good estimations of the decision boundary, even if Hopfield Boosting only samples a small number of weak learners. This is desirable because the AUX data contains a large number of data instances that are uninformative for the OOD detection task. For small, low dimensional data, one can always use all the data to compute E_b (Figure 2, a). For large problems, this strategy is difficult, and the naive solution of uniformly sampling N data points would also not work. This will yield many uninformative points (Figure 2, b). When using Hopfield Boosting and sampling N weak learners according to w_t , the result better approximates the decision boundary of the full data (Figure 2, c).

4.2. Data & Setup

CIFAR-10 We train Hopfield Boosting with ResNet-18 (He et al., 2016) on the CIFAR-10 data set (Krizhevsky, 2009). We use ImageNet-RC (Chrabaszcz et al., 2017) (a low-resolution version of ImageNet) as the AUX data. For testing the OOD detection performance, we use the data sets SVHN (Netzer et al., 2011), Textures (Cimpoi et al., 2014), iSUN (Xu et al., 2015), Places 365 (López-Cifuentes et al., 2020), and two versions of the LSUN data set (Yu et al., 2015) — one where the images are cropped, and one where they are resized to match the resolution of the CIFAR data sets (32x32 pixels). We evaluate the discriminative power of $s(\xi)$ between CIFAR and the respective OOD data set using the FPR95 and the AUROC.

Table 1: OOD detection performance on CIFAR-10. We compare results from Hopfield Boosting, POEM (Ming et al., 2022), EBO-OE (Liu et al., 2020), and MSP-OE (Hendrycks et al., 2019b) on ResNet-18. \downarrow indicates “lower is better” and \uparrow “higher is better”. All values in %. Standard deviations are estimated across five training runs.

OOD Data	Metric	HB (ours)	POEM	EBO-OE	MSP-OE
SVHN	FPR95 \downarrow	0.23\pm0.08	1.48 \pm 0.68	2.66 \pm 0.91	4.31 \pm 1.10
	AUROC \uparrow	99.57\pm0.06	99.33 \pm 0.15	99.15 \pm 0.23	99.20 \pm 0.15
LSUN-C	FPR95 \downarrow	0.82 \pm 0.17	4.02 \pm 0.91	6.82 \pm 0.74	7.02 \pm 1.14
	AUROC \uparrow	99.40 \pm 0.04	98.89 \pm 0.15	98.43 \pm 0.10	98.83 \pm 0.15
LSUN-R	FPR95 \downarrow	0.00\pm0.00	0.00\pm0.00	0.00\pm0.00	0.00\pm0.00
	AUROC \uparrow	99.98 \pm 0.02	99.88 \pm 0.12	99.98 \pm 0.02	99.96 \pm 0.00
Textures	FPR95 \downarrow	0.16\pm0.02	0.49 \pm 0.04	1.11 \pm 0.17	2.29 \pm 0.16
	AUROC \uparrow	99.84\pm0.01	99.72 \pm 0.05	99.61 \pm 0.02	99.57 \pm 0.01
iSUN	FPR95 \downarrow	0.00\pm0.00	0.00\pm0.00	0.00\pm0.00	0.00\pm0.00
	AUROC \uparrow	99.97 \pm 0.02	99.87 \pm 0.12	99.98 \pm 0.01	99.96 \pm 0.00
Places 365	FPR95 \downarrow	4.28\pm0.23	7.70 \pm 0.68	11.77 \pm 0.68	21.42 \pm 0.88
	AUROC \uparrow	98.51\pm0.10	97.56 \pm 0.26	96.39 \pm 0.30	95.91 \pm 0.17
Mean	FPR95 \downarrow	0.92	2.28	3.73	5.84
	AUROC \uparrow	99.55	99.21	98.92	98.90

Training. The network trains for 100 epochs. Each epoch, the model sees the entire ID data set and a selection of AUX samples. We evaluate the composite loss from Equation (7) for each mini-batch and update the model accordingly. After an epoch, we update the sample weights, yielding w_{t+1} . During the sample weight update, Hopfield Boosting does not compute gradients. The update of the sample weights w_{t+1} proceeds as follows: First, we fill the memories \mathbf{X} and \mathbf{O} with 50,000 samples, respectively. Second, we use the obtained \mathbf{X} and \mathbf{O} to get the energy $E_b(\Xi; \mathbf{X}, \mathbf{O})$ for 500,000 AUX samples and compute w_{t+1} according to Equation (6). In the following epoch, we sample the mini-batches \mathcal{O}_s^D according to w_{t+1} with replacement.

4.3. Results & Discussion

Table 1 summarizes the results for CIFAR-10. Hopfield Boosting surpasses POEM, improving the mean FPR95 metric from 2.28 to 0.92.

We also explore the influence of boosting (Table 6): The experiment shows that sampling weak learners contributes considerably to the performance of Hopfield Boosting. Although Hopfield Boosting shows superior performance compared to POEM even without boosting, outlier sampling can beat this version on every dataset on the FPR95 metric.

5. Conclusions

We introduce Hopfield Boosting: a method for OOD detection with OE. Hopfield Boosting uses an energy term to *boost* a classifier between inlier and outlier data by sampling weak learners that are close to the decision boundary. We compare Hopfield Boosting to three OOD detection approaches. Overall, Hopfield Boosting shows the best results.

Acknowledgements

We thank Christian Huber for helpful feedback and fruitful discussions.

The ELLIS Unit Linz, the LIT AI Lab, the Institute for Machine Learning, are supported by the Federal State Upper Austria. We thank the projects AI-MOTION (LIT-2018-6-YOU-212), DeepFlood (LIT-2019-8-YOU-213), Medical Cognitive Computing Center (MC3), INCONTROL-RL (FFG-881064), PRIMAL (FFG-873979), S3AI (FFG-872172), DL for GranularFlow (FFG-871302), EPILEPSIA (FFG-892171), AIRI FG 9-N (FWF-36284, FWF-36235), AI4GreenHeatingGrids(FFG- 899943), INTEGRATE (FFG-892418), ELISE (H2020-ICT-2019-3 ID: 951847), Stars4Waters (HORIZON-CL6-2021-CLIMATE-01-01). We thank Audi.JKU Deep Learning Center, TGW LOGISTICS GROUP GMBH, Silicon Austria Labs (SAL), University SAL Labs initiative, FILL Gesellschaft mbH, Anyline GmbH, Google, ZF Friedrichshafen AG, Robert Bosch GmbH, UCB Biopharma SRL, Merck Healthcare KGaA, Verbund AG, GLS (Univ. Waterloo) Software Competence Center Hagenberg GmbH, TÜV Austria, Frauscher Sensonic, Borealis AG, TRUMPF and the NVIDIA Corporation. This work has been supported by the "University SAL Labs" initiative of Silicon Austria Labs (SAL) and its Austrian partner universities for applied fundamental research for electronic-based systems. We acknowledge EuroHPC Joint Undertaking for awarding us access to Karolina at IT4Innovations, Czech Republic and Leonardo at CINECA, Italy.

References

- Abbott, L. F. and Arian, Y. Storage capacity of generalized networks. *Physical review A*, 36(10):5091, 1987.
- Ahn, S., Korattikara, A., and Welling, M. Bayesian posterior sampling via stochastic gradient Fisher scoring. In *Proceedings of the 29th International Conference on International Conference on Machine Learning*, pp. 1771–1778, Madison, WI, USA, 2012. Omnipress.
- Baldi, P. and Venkatesh, S. S. Number of stable points for spin-glasses and neural networks of higher orders. *Physical Review Letters*, 58(9):913, 1987.
- Caputo, B. and Niemann, H. Storage capacity of kernel associative memories. In *Artificial Neural Networks—ICANN 2002: International Conference Madrid, Spain, August 28–30, 2002 Proceedings 12*, pp. 51–56. Springer, 2002.
- Chen, H., Lee, Y., Sun, G., Lee, H., Maxwell, T., and Giles, C. L. High order correlation model for associative memory. In *AIP Conference Proceedings*, volume 151, pp. 86–99. American Institute of Physics, 1986.
- Chen, T., Kornblith, S., Norouzi, M., and Hinton, G. A simple framework for contrastive learning of visual representations. In *International conference on machine learning*, pp. 1597–1607. PMLR, 2020.
- Chrabaszcz, P., Loshchilov, I., and Hutter, F. A downsampled variant of imagenet as an alternative to the CIFAR datasets. *arXiv preprint arXiv:1707.08819*, 2017.
- Cimpoi, M., Maji, S., Kokkinos, I., Mohamed, S., and Vedaldi, A. Describing textures in the wild. In *Proceedings of the IEEE Conf. on Computer Vision and Pattern Recognition (CVPR)*, 2014.
- Cortes, C. and Vapnik, V. Support-vector networks. *Machine learning*, 20(3):273–297, 1995.
- Djurisic, A., Bozanic, N., Ashok, A., and Liu, R. Extremely simple activation shaping for out-of-distribution detection. In *The Eleventh International Conference on Learning Representations*, 2023.
- Freund, Y. and Schapire, R. E. A decision-theoretic generalization of on-line learning and an application to boosting. In *Computational Learning Theory: Eurocolt '95*, pp. 23–37. Springer-Verlag, 1995.
- Fürst, A., Rumetshofer, E., Lehner, J., Tran, V. T., Tang, F., Ramsauer, H., Kreil, D., Kopp, M., Klambauer, G., Bitto, A., et al. CLOOB: Modern Hopfield networks with InfoLOOB outperform clip. *Advances in neural information processing systems*, 35:20450–20468, 2022.
- Gardner, E. Multiconnected neural network models. *Journal of Physics A: Mathematical and General*, 20(11):3453, 1987.
- He, K., Zhang, X., Ren, S., and Sun, J. Deep residual learning for image recognition. In *Proceedings of the IEEE conference on computer vision and pattern recognition*, pp. 770–778, 2016.
- He, K., Fan, H., Wu, Y., Xie, S., and Girshick, R. Momentum contrast for unsupervised visual representation learning. In *Proceedings of the IEEE/CVF conference on computer vision and pattern recognition*, pp. 9729–9738, 2020.
- Hendrycks, D. and Gimpel, K. A baseline for detecting misclassified and out-of-distribution examples in neural networks. In *International Conference on Learning Representations*, 2017. URL <https://openreview.net/forum?id=Hkg4TI9xl>.
- Hendrycks, D., Basart, S., Mazeika, M., Zou, A., Kwon, J., Mostajabi, M., Steinhardt, J., and Song, D. Scaling out-of-distribution detection for real-world settings. *arXiv preprint arXiv:1911.11132*, 2019a.
- Hendrycks, D., Mazeika, M., and Dietterich, T. Deep anomaly detection with outlier exposure. In *International Conference on Learning Representations*, 2019b. URL <https://openreview.net/forum?id=HyxCxhRcY7>.

- Hopfield, J. J. Neural networks and physical systems with emergent collective computational abilities. *Proceedings of the National Academy of Sciences*, 79(8):2554–2558, 1982.
- Hopfield, J. J. Neurons with graded response have collective computational properties like those of two-state neurons. *Proceedings of the National Academy of Sciences*, 81(10):3088–3092, 1984. doi: 10.1073/pnas.81.10.3088.
- Horn, D. and Usher, M. Capacities of multiconnected memory models. *Journal de Physique*, 49(3):389–395, 1988.
- Isola, P., Xiao, J., Torralba, A., and Oliva, A. What makes an image memorable? In *CVPR 2011*, pp. 145–152. IEEE, 2011.
- Jiang, W., Cheng, H., Chen, M., Wang, C., and Wei, H. DOS: Diverse outlier sampling for out-of-distribution detection. In *The Twelfth International Conference on Learning Representations*, 2024. URL <https://openreview.net/forum?id=iriEqxFB4y>.
- Krizhevsky, A. Learning multiple layers of features from tiny images. Master’s thesis, Department of Computer Science, University of Toronto, 2009.
- Krotov, D. and Hopfield, J. J. Dense associative memory for pattern recognition. In Lee, D. D., Sugiyama, M., Luxburg, U. V., Guyon, I., and Garnett, R. (eds.), *Advances in Neural Information Processing Systems*, pp. 1172–1180. Curran Associates, Inc., 2016.
- LeCun, Y., Bottou, L., Bengio, Y., and Haffner, P. Gradient-based learning applied to document recognition. *Proceedings of the IEEE*, 86(11):2278–2324, 1998.
- Liu, W., Wang, X., Owens, J., and Li, Y. Energy-based out-of-distribution detection. In Larochelle, H., Ranzato, M., Hadsell, R., Balcan, M., and Lin, H. (eds.), *Advances in Neural Information Processing Systems*, volume 33, pp. 21464–21475. Curran Associates, Inc., 2020. URL <https://proceedings.neurips.cc/paper/2020/file/f5496252609c43eb8a3d147ab9b9c006-Paper.pdf>.
- Liu, X., Lochman, Y., and Zach, C. Gen: Pushing the limits of softmax-based out-of-distribution detection. In *Proceedings of the IEEE/CVF Conference on Computer Vision and Pattern Recognition*, pp. 23946–23955, 2023.
- López-Cifuentes, A., Escudero-Vinolo, M., Bescós, J., and García-Martín, Á. Semantic-aware scene recognition. *Pattern Recognition*, 102:107256, 2020.
- Loshchilov, I. and Hutter, F. Sgdr: Stochastic gradient descent with warm restarts. *arXiv preprint arXiv:1608.03983*, 2016.
- Lu, H., Gong, D., Wang, S., Xue, J., Yao, L., and Moore, K. Learning with mixture of prototypes for out-of-distribution detection. In *The Twelfth International Conference on Learning Representations*, 2024. URL <https://openreview.net/forum?id=uNkKaD3MCs>.
- McInnes, L., Healy, J., and Melville, J. Umap: Uniform manifold approximation and projection for dimension reduction. *arXiv preprint arXiv:1802.03426*, 2018.
- Ming, Y., Fan, Y., and Li, Y. POEM: Out-of-distribution detection with posterior sampling. In Chaudhuri, K., Jegelka, S., Song, L., Szepesvari, C., Niu, G., and Sabato, S. (eds.), *Proceedings of the 39th International Conference on Machine Learning*, volume 162 of *Proceedings of Machine Learning Research*, pp. 15650–15665. PMLR, 17–23 Jul 2022. URL <https://proceedings.mlr.press/v162/ming22a.html>.
- Moody, J. and Darken, C. J. Fast learning in networks of locally-tuned processing units. *Neural computation*, 1(2):281–294, 1989.
- Netzer, Y., Wang, T., Coates, A., Bissacco, A., Wu, B., and Ng, A. Y. Reading digits in natural images with unsupervised feature learning. 2011.
- Oord, A. v. d., Li, Y., and Vinyals, O. Representation learning with contrastive predictive coding. *arXiv preprint arXiv:1807.03748*, 2018.
- Park, G. Y., Kim, J., Kim, B., Lee, S. W., and Ye, J. C. Energy-based cross attention for Bayesian context update in text-to-image diffusion models. In *Thirty-seventh Conference on Neural Information Processing Systems*, 2023.
- Psaltis, D. and Park, C. H. Nonlinear discriminant functions and associative memories. In *AIP conference Proceedings*, volume 151, pp. 370–375. American Institute of Physics, 1986.
- Ramsauer, H., Schäfl, B., Lehner, J., Seidl, P., Widrich, M., Gruber, L., Holzleitner, M., Pavlović, M., Sandve, G. K., Greiff, V., Kreil, D., Kopp, M., Klambauer, G., Brandstetter, J., and Hochreiter, S. Hopfield networks is all you need. In *9th International Conference on Learning Representations (ICLR)*, 2021. URL <https://openreview.net/forum?id=tL89RnzIiCd>.
- Rätsch, G., Onoda, T., and Müller, K.-R. Soft margins for AdaBoost. *Machine learning*, 42:287–320, 2001.
- Ridnik, T., Ben-Baruch, E., Noy, A., and Zelnik-Manor, L. Imagenet-21k pretraining for the masses. In *Thirty-fifth Conference on Neural Information Processing Systems Datasets and Benchmarks Track (Round 1)*, 2021.
- Ruff, L., Kauffmann, J. R., Vandermeulen, R. A., Montavon, G., Samek, W., Kloft, M., Dietterich, T. G., and Müller, K.-R. A unifying review of deep and shallow anomaly detection. *Proceedings of the IEEE*, 109(5):756–795, 2021.

- Russakovsky, O., Deng, J., Su, H., Krause, J., Satheesh, S., Ma, S., Huang, Z., Karpathy, A., Khosla, A., Bernstein, M., et al. Imagenet large scale visual recognition challenge. *International journal of computer vision*, 115: 211–252, 2015.
- Saleh, R. A. and Saleh, A. Statistical properties of the log-cosh loss function used in machine learning. *arXiv preprint arXiv:2208.04564*, 2022.
- Schäfl, B., Gruber, L., Bitto-Nemling, A., and Hochreiter, S. Hopular: Modern Hopfield networks for tabular data. *arXiv preprint arXiv:2206.00664*, 2022.
- Sehwag, V., Chiang, M., and Mittal, P. Ssd: A unified framework for self-supervised outlier detection. *arXiv preprint arXiv:2103.12051*, 2021.
- smeschke. Four Shapes. <https://www.kaggle.com/datasets/smeschke/four-shapes/>, 2018. URL <https://www.kaggle.com/datasets/smeschke/four-shapes/>.
- Sun, Y., Guo, C., and Li, Y. React: Out-of-distribution detection with rectified activations. *Advances in Neural Information Processing Systems*, 34:144–157, 2021.
- Tao, L., Du, X., Zhu, X., and Li, Y. Non-parametric outlier synthesis. *arXiv preprint arXiv:2303.02966*, 2023.
- Teh, Y. W., Thiery, A. H., and Vollmer, S. J. Consistency and fluctuations for stochastic gradient Langevin dynamics. *J. Mach. Learn. Res.*, 17(1):193–225, 2016.
- Van Horn, G., Mac Aodha, O., Song, Y., Cui, Y., Sun, C., Shepard, A., Adam, H., Perona, P., and Belongie, S. The inaturalist species classification and detection dataset. In *Proceedings of the IEEE conference on computer vision and pattern recognition*, pp. 8769–8778, 2018.
- Vaswani, A., Shazeer, N., Parmar, N., Uszkoreit, J., Jones, L., Gomez, A. N., Kaiser, L., and Polosukhin, I. Attention is all you need. In Guyon, I., Luxburg, U. V., Bengio, S., Wallach, H., Fergus, R., Vishwanathan, S., and Garnett, R. (eds.), *Advances in Neural Information Processing Systems 30*, pp. 5998–6008. Curran Associates, Inc., 2017.
- Wang, Q., Fang, Z., Zhang, Y., Liu, F., Li, Y., and Han, B. Learning to augment distributions for out-of-distribution detection. In *NeurIPS, 2023a*. URL <https://openreview.net/forum?id=OtU6VvXJue>.
- Wang, Q., Ye, J., Liu, F., Dai, Q., Kalander, M., Liu, T., Hao, J., and Han, B. Out-of-distribution detection with implicit outlier transformation. *arXiv preprint arXiv:2303.05033*, 2023b.
- Wang, T. and Isola, P. Understanding contrastive representation learning through alignment and uniformity on the hypersphere. In *International Conference on Machine Learning*, pp. 9929–9939. PMLR, 2020.
- Wei, X.-S., Cui, Q., Yang, L., Wang, P., Liu, L., and Yang, J. Rpc: a large-scale and fine-grained retail product check-out dataset, 2022. URL <https://rpc-dataset.github.io/>.
- Welling, M. and Teh, Y. W. Bayesian learning via stochastic gradient Langevin dynamics. In *Proceedings of the 28th International Conference on Machine Learning*, pp. 681–688, Madison, WI, USA, 2011. Omnipress.
- Xu, P., Ehinger, K. A., Zhang, Y., Finkelstein, A., Kulkarini, S. R., and Xiao, J. Turkergaze: Crowdsourcing saliency with webcam based eye tracking. *arXiv preprint arXiv:1504.06755*, 2015.
- Xu, P., Chen, J., Zou, D., and Gu, Q. Global convergence of Langevin dynamics based algorithms for nonconvex optimization. In Bengio, S., Wallach, H., Larochelle, H., Grauman, K., Cesa-Bianchi, N., and Garnett, R. (eds.), *Advances in Neural Information Processing Systems*, volume 31, pp. 3122–3133. Curran Associates, Inc., 2018.
- Yang, J., Wang, P., Zou, D., Zhou, Z., Ding, K., Peng, W., Wang, H., Chen, G., Li, B., Sun, Y., et al. Openood: Benchmarking generalized out-of-distribution detection. *Advances in Neural Information Processing Systems*, 35: 32598–32611, 2022.
- Yu, F., Seff, A., Zhang, Y., Song, S., Funkhouser, T., and Xiao, J. LSUN: Construction of a large-scale image dataset using deep learning with humans in the loop. *arXiv preprint arXiv:1506.03365*, 2015.
- Yun, S., Han, D., Oh, S. J., Chun, S., Choe, J., and Yoo, Y. Cutmix: Regularization strategy to train strong classifiers with localizable features. In *Proceedings of the IEEE/CVF international conference on computer vision*, pp. 6023–6032, 2019.
- Zhang, H., Cisse, M., Dauphin, Y. N., and Lopez-Paz, D. mixup: Beyond empirical risk minimization. In *International Conference on Learning Representations*, 2018.
- Zhang, J., Fu, Q., Chen, X., Du, L., Li, Z., Wang, G., Han, S., Zhang, D., et al. Out-of-distribution detection based on in-distribution data patterns memorization with modern Hopfield energy. In *The Eleventh International Conference on Learning Representations*, 2023a.
- Zhang, J., Inkawhich, N., Linderman, R., Chen, Y., and Li, H. Mixture outlier exposure: Towards out-of-distribution detection in fine-grained environments. In *Proceedings of the IEEE/CVF Winter Conference on Applications of Computer Vision (WACV)*, pp. 5531–5540, January 2023b.
- Zhang, R., Li, C., Zhang, J., Chen, C., and Wilson, A. G. Cyclical stochastic gradient MCMC for Bayesian deep learning. In *International Conference on Learning Representations*, 2020.

Zheng, Y., Zhao, Y., Ren, M., Yan, H., Lu, X., Liu, J., and Li, J. Cartoon face recognition: A benchmark dataset. In *Proceedings of the 28th ACM International Conference on Multimedia*, pp. 2264–2272, 2020.

Zhu, J., Geng, Y., Yao, J., Liu, T., Niu, G., Sugiyama, M., and Han, B. Diversified outlier exposure for out-of-distribution detection via informative extrapolation. *Advances in Neural Information Processing Systems*, 36, 2023.

A. Details on Continuous Modern Hopfield Networks

The following arguments are adopted from [Fürst et al. \(2022\)](#) and [Ramsauer et al. \(2021\)](#). Associative memory networks have been designed to store and retrieve samples. Hopfield networks are energy-based, binary associative memories, which were popularized as artificial neural network architectures in the 1980s ([Hopfield, 1982, 1984](#)). Their storage capacity can be considerably increased by polynomial terms in the energy function ([Chen et al., 1986](#); [Psaltis & Park, 1986](#); [Baldi & Venkatesh, 1987](#); [Gardner, 1987](#); [Abbott & Arian, 1987](#); [Horn & Usher, 1988](#); [Caputo & Niemann, 2002](#); [Krotov & Hopfield, 2016](#)). In contrast to these binary memory networks, we use continuous associative memory networks with far higher storage capacity. These networks are continuous and differentiable, retrieve with a single update, and have exponential storage capacity (and are therefore scalable, i.e., able to tackle large problems; [Ramsauer et al., 2021](#)).

Formally, we denote a set of patterns $\{\mathbf{x}_1, \dots, \mathbf{x}_N\} \subset \mathbb{R}^d$ that are stacked as columns to the matrix $\mathbf{X} = (\mathbf{x}_1, \dots, \mathbf{x}_N)$ and a state pattern (query) $\boldsymbol{\xi} \in \mathbb{R}^d$ that represents the current state. The largest norm of a stored pattern is $M = \max_i \|\mathbf{x}_i\|$. Then, the energy E of continuous Modern Hopfield Networks with state $\boldsymbol{\xi}$ is defined as ([Ramsauer et al., 2021](#))

$$E = -\beta^{-1} \log \left(\sum_{i=1}^N \exp(\beta \mathbf{x}_i^T \boldsymbol{\xi}) \right) + \frac{1}{2} \boldsymbol{\xi}^T \boldsymbol{\xi} + C, \quad (10)$$

where $C = \beta^{-1} \log N + \frac{1}{2} M^2$. For energy E and state $\boldsymbol{\xi}$, [Ramsauer et al. \(2021\)](#) proved that the update rule

$$\boldsymbol{\xi}^{\text{new}} = \mathbf{X} \text{softmax}(\beta \mathbf{X}^T \boldsymbol{\xi}) \quad (11)$$

converges globally to stationary points of the energy E and coincides with the attention mechanisms of Transformers ([Vaswani et al., 2017](#); [Ramsauer et al., 2021](#)).

The *separation* Δ_i of a pattern \mathbf{x}_i is its minimal dot product difference to any of the other patterns:

$$\Delta_i = \min_{j, j \neq i} (\mathbf{x}_i^T \mathbf{x}_i - \mathbf{x}_i^T \mathbf{x}_j). \quad (12)$$

A pattern is *well-separated* from the data if Δ_i is above a given threshold (specified in [Ramsauer et al., 2021](#)). If the patterns \mathbf{x}_i are well-separated, the update rule Equation 11 converges to a fixed point close to a stored pattern. If some patterns are similar to one another and, therefore, not well-separated, the update rule converges to a fixed point close to the mean of the similar patterns.

The update rule of a Hopfield network thus identifies sample-sample relations between stored patterns. This enables similarity-based learning methods like nearest neighbor search (see [Schäfl et al., 2022](#)), which Hopfield Boosting leverages to detect samples outside the distribution of the training data.

B. Notes on Langevin Sampling

Another method that is appropriate for earlier acquired models is to sample the posterior via the Stochastic Gradient Langevin Dynamics (SGLD) ([Welling & Teh, 2011](#)). This method is efficient since it iteratively learns from small mini-batches [Welling & Teh \(2011\)](#); [Ahn et al. \(2012\)](#). See basic work on Langevin dynamics [Welling & Teh \(2011\)](#); [Ahn et al. \(2012\)](#); [Teh et al. \(2016\)](#); [Xu et al. \(2018\)](#). A cyclical stepsize schedule for SGLD was very promising for uncertainty quantification [Zhang et al. \(2020\)](#). Larger steps discover new modes, while smaller steps characterize each mode and perform the posterior sampling.

C. Related work

C.1. Details on further OE approaches

This section gives details about related works from the area of OE in OOD detection. With OE, we refer to the usage of AUX for training an OOD detector in general.

MSP-OE. [Hendrycks et al. \(2019b\)](#) were the first to introduce the term OE in the context of OOD detection. Specifically, they improve an MSP-based OOD detection ([Hendrycks & Gimpel, 2017](#)): They train a classifier on the ID data set and maximize the entropy of the predictive distribution of the classifier for the AUX data. The combined loss they employ is

$$\mathcal{L} = \mathcal{L}_{\text{CE}} + \lambda \mathcal{L}_{\text{OOD}} \quad (13)$$

$$\mathcal{L}_{\text{OOD}} = \mathbb{E}_{\mathbf{o}^{\mathcal{D}} \sim p_{\text{AUX}}} [H(\mathcal{U}, p_{\theta}(\mathbf{o}))] \quad (14)$$

where H denotes the cross-entropy, \mathcal{U} denotes the uniform distribution over K classes, and p_{θ} is the model mapping the features to the predictive distribution over the K classes.

EBO-OE. Liu et al. (2020) propose a post-hoc and an OE approach. Their post-hoc approach (EBO) is to use the classifier’s energy to perform OOD detection:

$$E(\xi^{\mathcal{D}}) = -\beta^{-1} \text{lse}(\beta, f_{\theta}(\xi^{\mathcal{D}})) \quad (15)$$

$$s(\xi^{\mathcal{D}}) = -E(\xi^{\mathcal{D}}, f_{\theta}) \quad (16)$$

where f_{θ} outputs the model’s logits as a vector. Their OE approach (EBO-OE) promotes a low energy on ID samples and a high energy on AUX samples:

$$\mathcal{L}_{\text{OOD}} = \mathbb{E}_{\mathbf{x}^{\mathcal{D}} \sim p_{\text{ID}}} [(\max(0, E(\mathbf{x}^{\mathcal{D}}) - m_{\text{ID}}))^2] + \mathbb{E}_{\mathbf{o}^{\mathcal{D}} \sim p_{\text{AUX}}} [(\max(0, m_{\text{AUX}} - E(\mathbf{o}^{\mathcal{D}}))]^2 \quad (17)$$

where m_{ID} and m_{AUX} are margin hyperparameters.

POEM. Ming et al. (2022) propose to incorporate Thompson sampling into the OE process. More specifically, they sample a linear decision boundary in embedding space between the ID and AUX data using Bayesian linear regression and then select those samples from the AUX data set that are closest to the sampled decision boundary. In the following epoch, they sample the AUX data uniformly from the selected data instances without replacement and optimize the model with the EBO-OE loss (Equation (17)).

MixOE. Zhang et al. (2023b) employ mixup (Zhang et al., 2018) between the ID and AUX samples to augment the OE task. Formally, this results in the following:

$$\tilde{\mathbf{x}} = \lambda \mathbf{x}^{\mathcal{D}} + (1 - \lambda) \mathbf{o}^{\mathcal{D}} \quad (18)$$

$$\tilde{y} = \lambda y + (1 - \lambda) \mathcal{U} \quad (19)$$

$$\mathcal{L}_{\text{OOD}} = \mathbb{E}_{\substack{(\mathbf{x}^{\mathcal{D}}, y) \sim p_{\text{ID}} \\ \mathbf{o}^{\mathcal{D}} \sim p_{\text{AUX}}}} [H(\tilde{y}, \tilde{\mathbf{x}})] \quad (20)$$

Alternatively, they also propose to employ CutMix (Yun et al., 2019) instead of mixup (which would change the mixing operation in Equation (18)).

DAL. Wang et al. (2023a) augment the AUX data by defining a Wasserstein-1 ball around the AUX data and performing OE using this Wasserstein ball. DAL is motivated by the concept of distribution discrepancy: The distribution of the real OOD data will in general be different from the distribution of the AUX data. The authors argue that their approach can make OOD detection more reliable if the distribution discrepancy is large.

DivOE. Zhu et al. (2023) pose the question of how to utilize the given outliers from the AUX data set if the auxiliary outliers are not informative enough to represent the unseen OOD distribution. They suggest solving this problem by diversifying the AUX data using extrapolation, which should result in better coverage of the OOD space of the resultant extrapolated distribution. Formally, they employ a loss using a synthesized distribution with a manipulation Δ :

$$\mathcal{L}_{\text{OOD}} = \mathbb{E}_{\mathbf{o}^{\mathcal{D}} \sim p_{\text{AUX}}} [(1 - \gamma)H(\mathcal{U}, p_{\theta}(\mathbf{o}^{\mathcal{D}})) + \gamma \max_{\Delta} [H(\mathcal{U}, p_{\theta}(\mathbf{o}^{\mathcal{D}} + \Delta)) - H(\mathcal{U}, p_{\theta}(\mathbf{o}^{\mathcal{D}}))]] \quad (21)$$

DOE. Wang et al. (2023b) implicitly synthesize auxiliary outlier data using a transformation of the model weights. They argue that perturbing the model parameters has the same effect as transforming the data.

DOS. Jiang et al. (2024) apply K-means clustering to the features of the AUX data set. They then employ a balanced sampling from the K obtained clusters by selecting the same number of samples from each cluster for training. More specifically, they select those n samples from each cluster which are closest to the decision boundary between the ID and OOD regions.

D. Societal Impact

This section discusses the potential positive and negative societal impacts of our work. As our work aims to improve the state-of-the-art in OOD detection, we focus on the potential societal impact of OOD detection in general.

• Positive Impacts

- **Improved model reliability:** OOD detection aims to detect unfamiliar inputs that have little support in the model’s training distribution. When these samples are detected, one can, for example, notify the user that no prediction is possible, or trigger a manual intervention. This can lead to an increase in a model’s reliability.
- **Abstain from doing uncertain predictions:** When a model with appropriate OOD detection recognizes that a query sample has limited support in the training distribution, it can abstain from performing a prediction. This can, for example, increase trust in ML models, as they will rather tell the user they are uncertain than report a confidently wrong prediction.

• Negative Impacts

- **Wrong sense of safety:** Having OOD detection in place could cause users to wrongly assume that all OOD inputs will be detected. However, like most systems, also OOD detection methods can make errors. It is important to consider that certain OOD examples could remain undetected.
- **Potential for misinterpretation:** As with many other ML systems, the outcomes of OOD detection methods are prone to misinterpretation. It is important to acquaint oneself with the respective method before applying it in practice.

E. Toy Examples

E.1. 3D Visualizations of E_b on a hypersphere

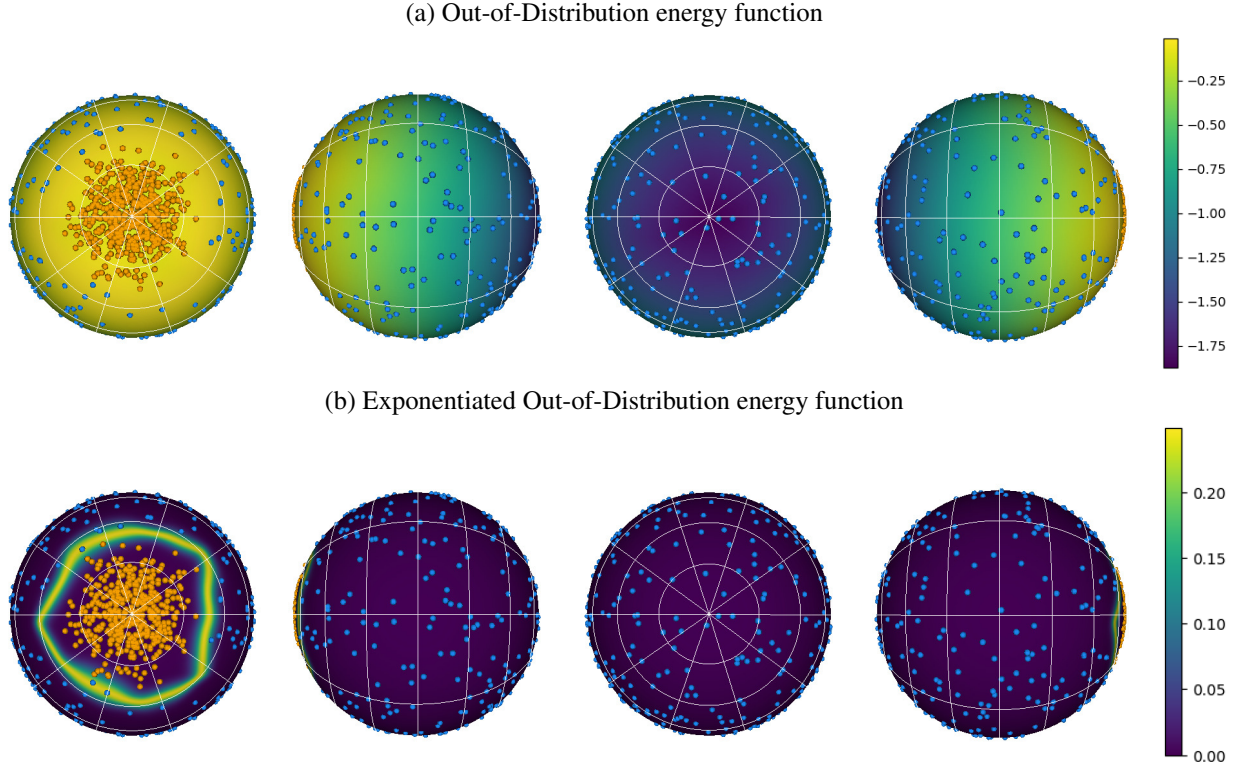


Figure 3: Depiction of the energy function $E_b(\xi; \mathbf{X}, \mathbf{O})$ on a hypersphere. (a) shows $E_b(\xi; \mathbf{X}, \mathbf{O})$ with exemplary inlier (orange) and outlier (blue) points; and (b) shows $\exp(\beta E_b(\xi; \mathbf{X}, \mathbf{O}))$. β was set to 128. Both, (a) and (b), rotate the sphere by 0, 90, 180, and 270 degrees around the vertical axis.

This example depicts how inliers and outliers shape the energy surface (Figure 3). We generated patterns so that \mathbf{X} clusters around a pole and the outliers populate the remaining perimeter of the sphere. This is analogous to the idea that one has access to a large AUX data set, where some data points are more and some less informative for OOD detection (e.g., as conceptualized in [Ming et al., 2022](#)).

E.2. Dynamics of \mathcal{L}_{OOD} on Patterns in Euclidean Space

In this example, we applied our out-of-distribution loss \mathcal{L}_{OOD} on a simple binary classification problem. As we are working in Euclidean space and not on a sphere, we use a modified version of MHE, which uses the negative squared Euclidean distance instead of the dot-product-similarity. For the formal relation between Equation (22) and MHE, we refer to Appendix G.1:

$$E(\xi; \mathbf{X}) = -\beta^{-1} \log \left(\sum_{i=1}^N \exp\left(-\frac{\beta}{2} \|\xi - \mathbf{x}_i\|_2^2\right) \right) \quad (22)$$

Figure 4a shows the initial state of the patterns and the decision boundary $\exp(\beta E_b(\xi; \mathbf{X}, \mathbf{O}))$. We store the samples of the two classes as stored patterns in \mathbf{X} and \mathbf{O} , respectively, and compute \mathcal{L}_{OOD} for all samples. We then set the learning rate to 0.1 and perform gradient descent with \mathcal{L}_{OOD} on the data points. Figure 4b shows that after 25 steps, the distance between the data points and the decision boundary has increased, especially for samples that had previously been close to the decision boundary. After 100 steps, as shown in Figure 4d, the variability orthogonal to the decision boundary has almost completely vanished, while the variability parallel to the decision boundary is maintained.

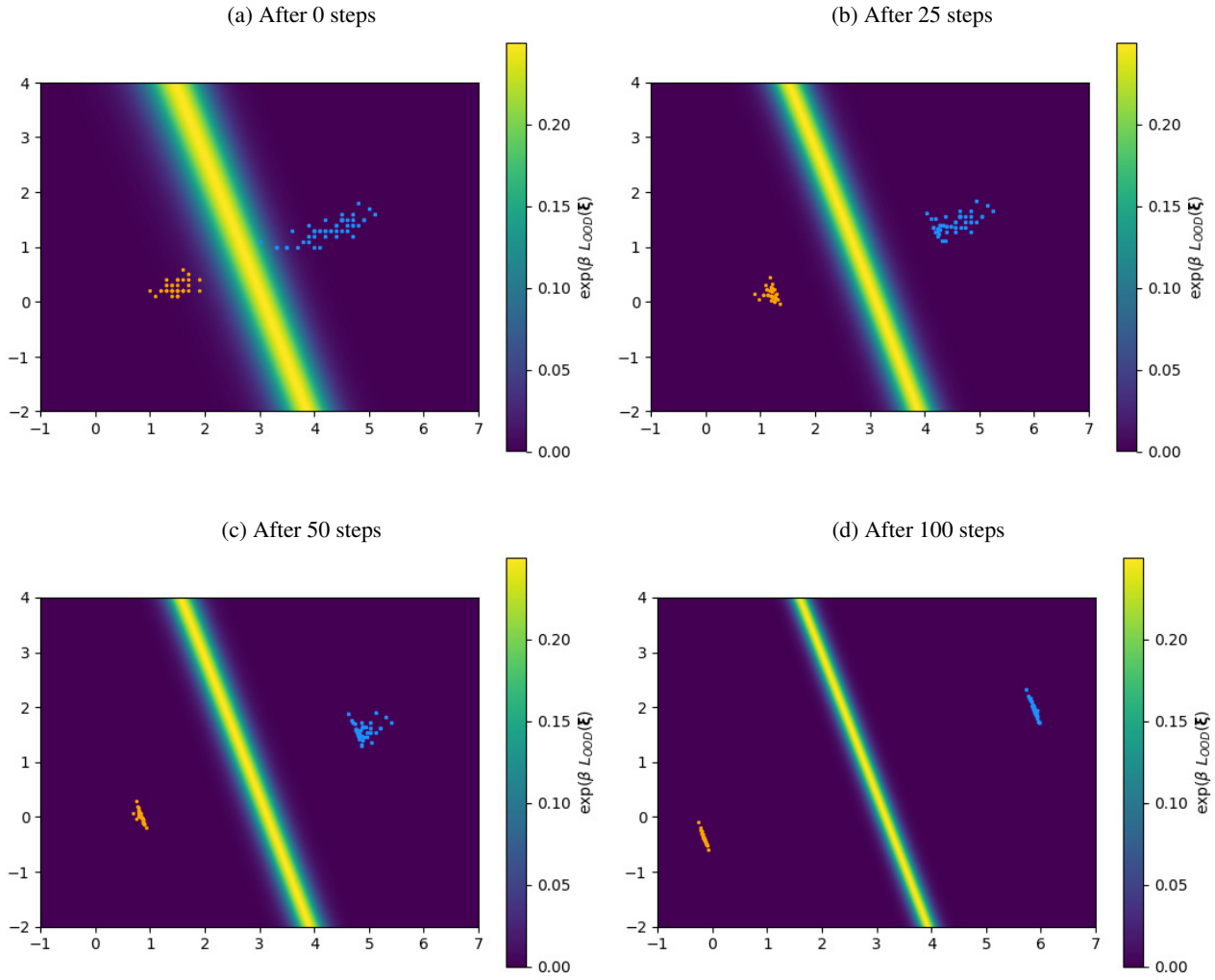


Figure 4: \mathcal{L}_{OOD} applied to exemplary data points on euclidean space. Gradient updates are applied to the data points directly. We observe that the variance orthogonal to the decision boundary shrinks while the variance parallel to the decision boundary does not change to this extent. β is set to 2.

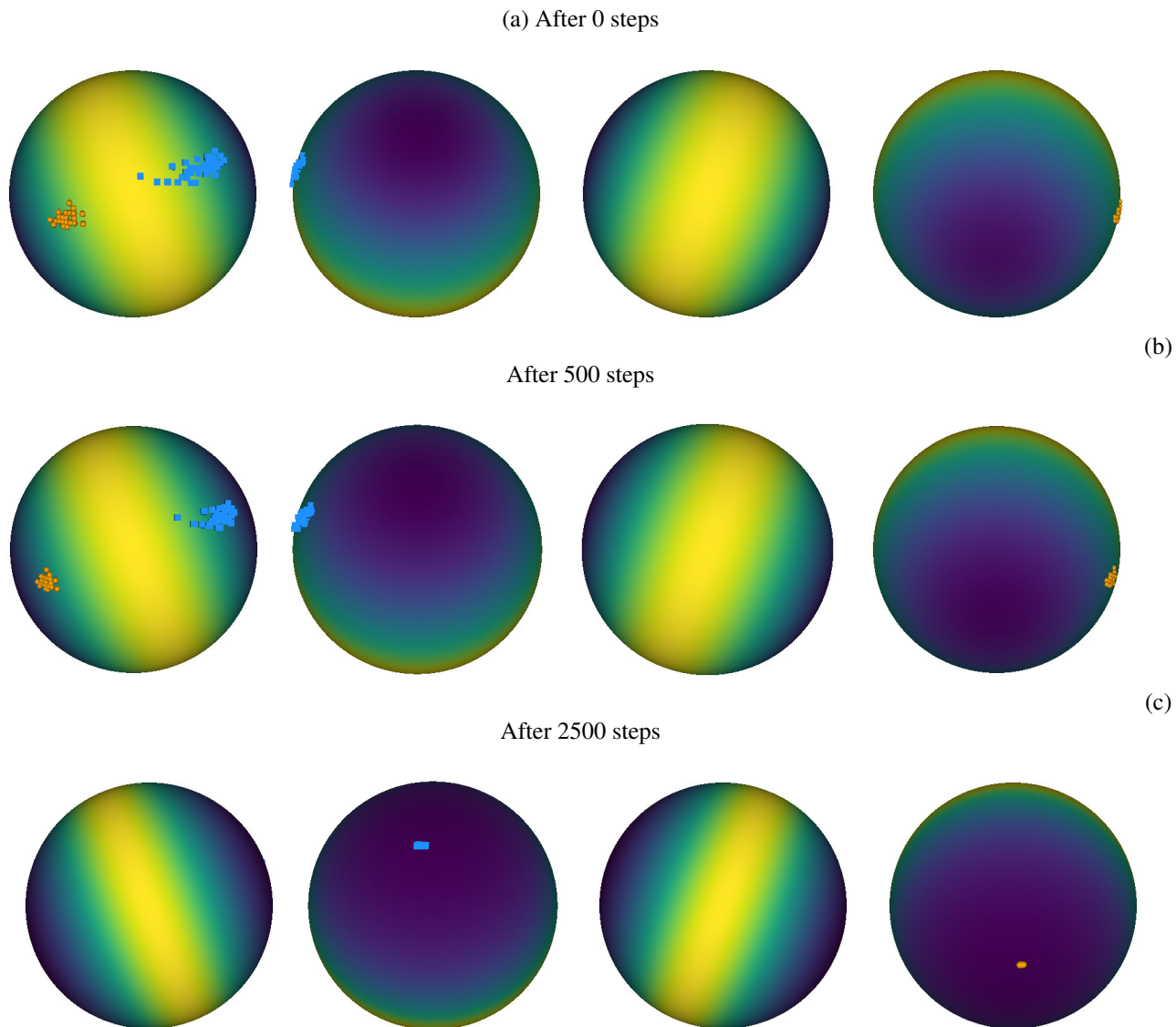
E.3. Dynamics of \mathcal{L}_{OOD} on Patterns on the Sphere

Figure 5: \mathcal{L}_{OOD} applied to exemplary data points on a sphere. Gradients are applied to the data points directly. We observe that the geometry of the space forces the patterns to opposing poles of the sphere.

E.4. Learning Dynamics of Hopfield Boosting on Patterns on a Sphere - Video

The example video¹ demonstrates the learning dynamics of Hopfield Boosting on a 3-dimensional sphere. We randomly generate ID patterns \mathbf{X} clustering around one of the sphere’s poles and AUX patterns \mathbf{O} on the remaining surface of the sphere. We then apply Hopfield Boosting on this data set. First, we sample the weak learners close to the decision boundary for both classes, \mathbf{X} and \mathbf{O} . Then, we perform 2000 steps of gradient descent with \mathcal{L}_{OOD} on the sampled weak learners. We apply the gradient updates to the patterns directly and do not propagate any gradients to an encoder. Every 50 gradient steps, we re-sample the weak learners. For this example, the initial learning rate is set to 0.02 and increased after every gradient step by 0.1%.

¹<https://youtu.be/4AB3tILdrvQ>

E.5. Location of Weak Learners near the Decision Boundary

A weak learner can be constructed from a sample close to the decision boundary as follows: Given the sample, we create a radial decision boundary centered on the sample. We now optimize one parameter (the radius of the decision boundary) to minimize the error on the training set. Our classifier is a weak learner because no matter how the radius is selected, the resulting hypothesis will likely only perform slightly better than random guessing.

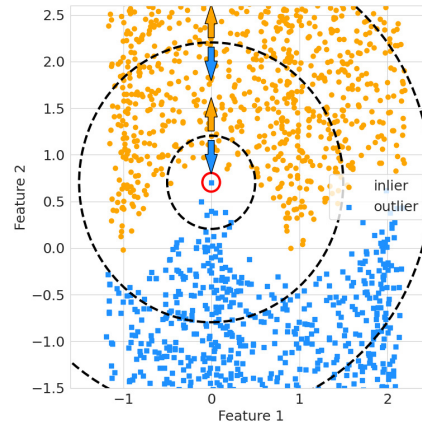


Figure 6: A prototypical classifier (red circle) that is constructed with a sample close to the decision boundary. Classifiers like this one will only perform slightly better than random guessing (as indicated by the radial decision boundaries) and are, therefore, well-suited for weak learners.

F. Notes on E_b

F.1. Probabilistic Interpretation of E_b

We model the class-conditional densities of the in-distribution data and auxiliary data as mixtures of Gaussians with the patterns as the component means and tied, diagonal covariance matrices with β^{-1} in the main diagonal.

$$p(\boldsymbol{\xi} | \text{ID}) = \frac{1}{N} \sum_{i=1}^N \mathcal{N}(\boldsymbol{\xi}; \mathbf{x}_i, \beta^{-1} \mathbf{I}) \quad (23)$$

$$p(\boldsymbol{\xi} | \text{AUX}) = \frac{1}{M} \sum_{i=1}^M \mathcal{N}(\boldsymbol{\xi}; \mathbf{o}_i, \beta^{-1} \mathbf{I}) \quad (24)$$

Further, we assume the distribution $p(\boldsymbol{\xi})$ as a mixture of $p(\boldsymbol{\xi} | \text{ID})$ and $p(\boldsymbol{\xi} | \text{AUX})$ with equal prior probabilities (mixture weights):

$$p(\boldsymbol{\xi}) = p(\text{ID}) p(\boldsymbol{\xi} | \text{ID}) + p(\text{AUX}) p(\boldsymbol{\xi} | \text{AUX}) \quad (25)$$

$$= \frac{1}{2} p(\boldsymbol{\xi} | \text{ID}) + \frac{1}{2} p(\boldsymbol{\xi} | \text{AUX}) \quad (26)$$

The probability of an unknown sample $\boldsymbol{\xi}$ being an AUX sample is given by

$$p(\text{AUX} | \boldsymbol{\xi}) = \frac{p(\boldsymbol{\xi} | \text{AUX}) p(\text{AUX})}{p(\boldsymbol{\xi})} \quad (27)$$

$$= \frac{p(\boldsymbol{\xi} | \text{AUX})}{2 p(\boldsymbol{\xi})} \quad (28)$$

$$= \frac{p(\boldsymbol{\xi} | \text{AUX})}{p(\boldsymbol{\xi} | \text{AUX}) + p(\boldsymbol{\xi} | \text{ID})} \quad (29)$$

$$= \frac{1}{1 + \frac{p(\boldsymbol{\xi} | \text{ID})}{p(\boldsymbol{\xi} | \text{AUX})}} \quad (30)$$

$$= \frac{1}{1 + \exp(\log(p(\boldsymbol{\xi} | \text{ID})) - \log(p(\boldsymbol{\xi} | \text{AUX})))} \quad (31)$$

where in line (30) we have used that $p(\boldsymbol{\xi} | \text{AUX}) > 0$ for all $\boldsymbol{\xi} \in \mathbb{R}^d$. The probability of $\boldsymbol{\xi}$ being an ID sample is given by

$$p(\text{ID} | \boldsymbol{\xi}) = \frac{p(\boldsymbol{\xi} | \text{ID})}{2 p(\boldsymbol{\xi})} \quad (32)$$

$$= \frac{1}{1 + \exp(\log(p(\boldsymbol{\xi} | \text{AUX})) - \log(p(\boldsymbol{\xi} | \text{ID})))} \quad (33)$$

$$= 1 - p(\text{AUX} | \boldsymbol{\xi}) \quad (34)$$

Consider the function

$$f_b(\boldsymbol{\xi}) = p(\text{AUX} | \boldsymbol{\xi}) \cdot p(\text{ID} | \boldsymbol{\xi}) \quad (35)$$

$$= \frac{p(\boldsymbol{\xi} | \text{AUX}) \cdot p(\boldsymbol{\xi} | \text{ID})}{4 p(\boldsymbol{\xi})^2} \quad (36)$$

By taking the log of Equation (36) we obtain the following. We use $\stackrel{C}{\equiv}$ to denote equality up to an additive constant that does not depend on ξ .

$$\beta^{-1} \log(f_b(\xi)) \stackrel{C}{\equiv} -2\beta^{-1} \log(p(\xi)) + \beta^{-1} \log(p(\xi | \text{ID})) + \beta^{-1} \log(p(\xi | \text{AUX})) \quad (37)$$

Pre-multiplication by β^{-1} is equivalent to a change of base of the log. The term $-\beta^{-1} \log(p(\xi))$ is equivalent to the MHE (Ramsauer et al., 2021) (up to an additive constant) when assuming normalized patterns, i.e. $\|\mathbf{x}_i\|_2 = 1$ and $\|\mathbf{o}_i\|_2 = 1$, and an equal number of patterns $M = N$ in the two Gaussian mixtures $p(\xi | \text{ID})$ and $p(\xi | \text{AUX})$:

$$-\beta^{-1} \log(p(\xi)) = -\beta^{-1} \log\left(\frac{1}{2}p(\xi | \text{ID}) + \frac{1}{2}p(\xi | \text{AUX})\right) \quad (38)$$

$$\stackrel{C}{\equiv} -\beta^{-1} \log(p(\xi | \text{ID}) + p(\xi | \text{AUX})) \quad (39)$$

$$= -\beta^{-1} \log\left(\frac{1}{N} \sum_{i=1}^N \mathcal{N}(\xi; \mathbf{x}_i, \beta^{-1} \mathbf{I}) + \frac{1}{N} \sum_{i=1}^N \mathcal{N}(\xi; \mathbf{o}_i, \beta^{-1} \mathbf{I})\right) \quad (40)$$

$$\stackrel{C}{\equiv} -\beta^{-1} \log\left(\sum_{i=1}^N \mathcal{N}(\xi; \mathbf{x}_i, \beta^{-1} \mathbf{I}) + \sum_{i=1}^N \mathcal{N}(\xi; \mathbf{o}_i, \beta^{-1} \mathbf{I})\right) \quad (41)$$

$$\stackrel{C}{\equiv} -\beta^{-1} \log\left(\sum_{i=1}^N \exp\left(-\frac{\beta}{2} \|\xi - \mathbf{x}_i\|_2^2\right) + \sum_{i=1}^N \exp\left(-\frac{\beta}{2} \|\xi - \mathbf{o}_i\|_2^2\right)\right) \quad (42)$$

$$\stackrel{C}{\equiv} -\beta^{-1} \log\left(\sum_{i=1}^N \exp\left(\beta \mathbf{x}_i^T \xi - \frac{\beta}{2} \xi^T \xi\right) + \sum_{i=1}^N \exp\left(\beta \mathbf{o}_i^T \xi - \frac{\beta}{2} \xi^T \xi\right)\right) \quad (43)$$

$$= -\beta^{-1} \log\left(\sum_{i=1}^N \exp(\beta \mathbf{x}_i^T \xi) + \sum_{i=1}^N \exp(\beta \mathbf{o}_i^T \xi)\right) + \frac{1}{2} \xi^T \xi \quad (44)$$

$$\stackrel{C}{\equiv} -\text{lse}(\beta, (\mathbf{X} \parallel \mathbf{O})^T \xi) + \frac{1}{2} \xi^T \xi + \beta^{-1} \log N + \frac{1}{2} M^2 \quad (45)$$

Analogously, $\beta^{-1} \log(p(\xi | \text{ID}))$ and $\beta^{-1} \log(p(\xi | \text{AUX}))$ also yield MHE terms. Therefore, E_b is equivalent to $\beta^{-1} \log(f_b(\xi))$ under the assumption that $\|\mathbf{x}_i\|_2 = 1$ and $\|\mathbf{o}_i\|_2 = 1$ and $M = N$. The $\frac{1}{2} \xi^T \xi$ terms that are contained in the three MHEs cancel out.

$$\beta^{-1} \log(f_b(\xi)) \stackrel{C}{\equiv} -2 \text{lse}(\beta, (\mathbf{X} \parallel \mathbf{O})^T \xi) + \text{lse}(\beta, \mathbf{X}^T \xi) + \text{lse}(\beta, \mathbf{O}^T \xi) = E_b(\xi; \mathbf{X}, \mathbf{O}) \quad (46)$$

$f_b(\xi)$ can also be interpreted as the variance of a Bernoulli distribution with outcomes ID and AUX:

$$f_b(\xi) = p(\text{AUX} | \xi) p(\text{ID} | \xi) = p(\text{ID} | \xi) (1 - p(\text{ID} | \xi)) = p(\text{AUX} | \xi) (1 - p(\text{AUX} | \xi)) \quad (47)$$

In other words, minimizing E_b means to drive a Bernoulli-distributed random variable with the outcomes ID and AUX towards minimum variance, i.e., $p(\text{ID} | \xi)$ is driven towards 1 if $p(\text{ID} | \xi) > 0.5$ and towards 0 if $p(\text{ID} | \xi) < 0.5$. Conversely, the same is true for $p(\text{AUX} | \xi)$.

From Equation (31), under the assumptions that $\|\mathbf{x}_i\|_2 = 1$ and $\|\mathbf{o}_i\|_2 = 1$ and $M = N$, the conditional probability $p(\text{AUX} | \xi)$ can be computed as follows:

$$p(\text{AUX} | \xi) = \sigma(\log(p(\xi | \text{AUX})) - \log(p(\xi | \text{ID}))) \quad (48)$$

$$= \sigma(\beta (\text{lse}(\beta, \mathbf{O}^T \xi) - \text{lse}(\beta, \mathbf{X}^T \xi))) \quad (49)$$

where σ denotes the logistic sigmoid function. Similarly, $p(\text{ID} \mid \boldsymbol{\xi})$ can be computed using

$$p(\text{ID} \mid \boldsymbol{\xi}) = \sigma(\beta (\text{lse}(\beta, \mathbf{X}^T \boldsymbol{\xi}) - \text{lse}(\beta, \mathbf{O}^T \boldsymbol{\xi}))) \quad (50)$$

$$= 1 - p(\text{AUX} \mid \boldsymbol{\xi}) \quad (51)$$

F.2. Alternative Formulations of E_b and f_b

E_b can be rewritten as follows.

$$E_b(\boldsymbol{\xi}; \mathbf{X}, \mathbf{O}) = -2 \text{lse}(\beta, (\mathbf{X} \parallel \mathbf{O})^T \boldsymbol{\xi}) + \text{lse}(\beta, \mathbf{X}^T \boldsymbol{\xi}) + \text{lse}(\beta, \mathbf{O}^T \boldsymbol{\xi}) \quad (52)$$

$$= -2\beta^{-1} \log \cosh \left(\frac{\beta}{2} (\text{lse}(\beta, \mathbf{X}^T \boldsymbol{\xi}) - \text{lse}(\beta, \mathbf{O}^T \boldsymbol{\xi})) \right) - 2\beta^{-1} \log(2) \quad (53)$$

To prove this, we first show the following:

$$- \beta^{-1} \log \left(\exp(\beta \text{lse}(\beta, \mathbf{X}^T \boldsymbol{\xi})) + \exp(\beta \text{lse}(\beta, \mathbf{O}^T \boldsymbol{\xi})) \right) \quad (54)$$

$$= - \beta^{-1} \log \left(\exp \left(\beta \beta^{-1} \log \left(\sum_{i=1}^N \exp(\beta \mathbf{x}_i^T \boldsymbol{\xi}) \right) \right) + \exp \left(\beta \beta^{-1} \log \left(\sum_{i=1}^N \exp(\beta \mathbf{o}_i^T \boldsymbol{\xi}) \right) \right) \right) \quad (55)$$

$$= - \beta^{-1} \log \left(\sum_{i=1}^N \exp(\beta \mathbf{x}_i^T \boldsymbol{\xi}) + \sum_{i=1}^N \exp(\beta \mathbf{o}_i^T \boldsymbol{\xi}) \right) \quad (56)$$

$$= - \text{lse}(\beta, (\mathbf{X} \parallel \mathbf{O})^T \boldsymbol{\xi}) \quad (57)$$

Let $E_{\mathbf{X}} = -\text{lse}(\beta, \mathbf{X}^T \boldsymbol{\xi})$ and $E_{\mathbf{O}} = -\text{lse}(\beta, \mathbf{O}^T \boldsymbol{\xi})$.

$$E_b(\boldsymbol{\xi}; \mathbf{X}, \mathbf{O}) = -2 \text{lse}(\beta, (\mathbf{X} \parallel \mathbf{O})^T \boldsymbol{\xi}) + \text{lse}(\beta, \mathbf{X}^T \boldsymbol{\xi}) + \text{lse}(\beta, \mathbf{O}^T \boldsymbol{\xi}) \quad (58)$$

$$= -2\beta^{-1} \log \left(\exp(-\beta E_{\mathbf{X}}) + \exp(-\beta E_{\mathbf{O}}) \right) - E_{\mathbf{X}} - E_{\mathbf{O}} \quad (59)$$

$$= -2\beta^{-1} \log \left(\exp\left(-\frac{\beta}{2} E_{\mathbf{X}}\right) + \exp\left(-\beta E_{\mathbf{O}} + \frac{\beta}{2} E_{\mathbf{X}}\right) \right) - E_{\mathbf{O}} \quad (60)$$

$$= -2\beta^{-1} \log \left(\exp\left(-\frac{\beta}{2} E_{\mathbf{X}} + \frac{\beta}{2} E_{\mathbf{O}}\right) + \exp\left(-\frac{\beta}{2} E_{\mathbf{O}} + \frac{\beta}{2} E_{\mathbf{X}}\right) \right) \quad (61)$$

$$= -2\beta^{-1} \log \cosh \left(\frac{\beta}{2} (-E_{\mathbf{X}} + E_{\mathbf{O}}) \right) - 2\beta^{-1} \log(2) \quad (62)$$

$$= -2\beta^{-1} \log \cosh \left(\frac{\beta}{2} (\text{lse}(\beta, \mathbf{X}^T \boldsymbol{\xi}) - \text{lse}(\beta, \mathbf{O}^T \boldsymbol{\xi})) \right) - 2\beta^{-1} \log(2) \quad (63)$$

$$= -2\beta^{-1} \log \cosh \left(\frac{\beta}{2} (\text{lse}(\beta, \mathbf{O}^T \boldsymbol{\xi}) - \text{lse}(\beta, \mathbf{X}^T \boldsymbol{\xi})) \right) - 2\beta^{-1} \log(2) \quad (64)$$

By exponentiation of the above result we obtain

$$f_b(\boldsymbol{\xi}) \propto \exp(\beta E_b(\boldsymbol{\xi}; \mathbf{X}, \mathbf{O})) = \frac{1}{4 \cosh^2 \left(\frac{\beta}{2} (\text{lse}(\beta, \mathbf{X}^T \boldsymbol{\xi}) - \text{lse}(\beta, \mathbf{O}^T \boldsymbol{\xi})) \right)} \quad (65)$$

The function $\log \cosh(x)$ is related to the negative log-likelihood of the hyperbolic secant distribution (see e.g. [Saleh & Saleh, 2022](#)). For values of x close to 0, $\log \cosh$ can be approximated by $\frac{x^2}{2}$, and for values far from 0, the function behaves as $|x| - \log(2)$.

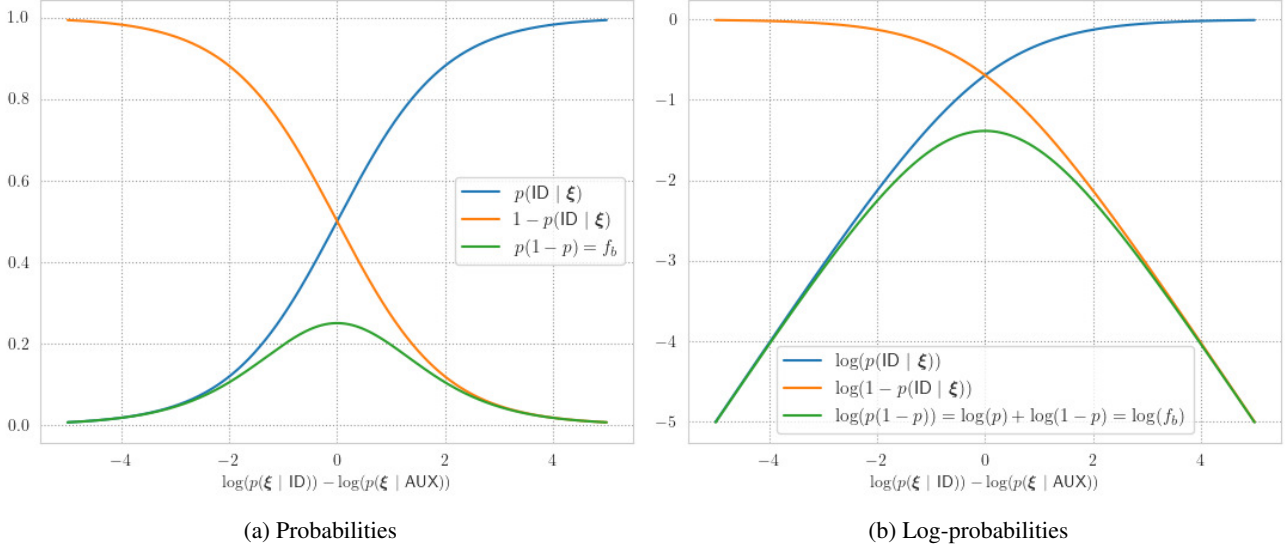


Figure 7: The product of two logistic sigmoids yields f_b (a); the sum of two log-sigmoids yields $\log(f_b) = E_b$ (b).

F.3. Derivatives of E_b

In this section, we investigate the derivatives of the energy function E_b . The derivative of the lse is:

$$\nabla_{\mathbf{z}} \text{lse}(\beta, \mathbf{z}) = \nabla_{\mathbf{z}} \beta^{-1} \log \left(\sum_{i=1}^N \exp(\beta z_i) \right) = \text{softmax}(\beta \mathbf{z}) \quad (66)$$

Thus, the derivative of the MHE $E(\xi; \mathbf{X})$ w.r.t. ξ is:

$$\nabla_{\xi} E(\xi; \mathbf{X}) = \nabla_{\xi} (-\text{lse}(\beta, \mathbf{X}^T \xi) + \frac{1}{2} \xi^T \xi + C) = -\mathbf{X} \text{softmax}(\beta \mathbf{X}^T \xi) + \xi \quad (67)$$

The update rule of the MHN

$$\xi^{t+1} = \mathbf{X} \text{softmax}(\beta \mathbf{X}^T \xi^t) \quad (68)$$

is derived via the concave-convex procedure. It coincides with the attention mechanisms of Transformers and has been proven to converge globally to stationary points of the energy $E(\xi; \mathbf{X})$ (Ramsauer et al., 2021). It can also be shown that the update rule emerges when performing gradient descent on $E(\xi; \mathbf{X})$ with step size $\eta = 1$ Park et al. (2023):

$$\xi^{t+1} = \xi^t - \eta \nabla_{\xi} E(\xi^t; \mathbf{X}) \quad (69)$$

$$\xi^{t+1} = \mathbf{X} \text{softmax}(\beta \mathbf{X}^T \xi^t) \quad (70)$$

From Equation (67), we can see that the gradient of $E_b(\xi; \mathbf{X}, \mathbf{O})$ w.r.t. ξ is:

$$\nabla_{\xi} E_b(\xi; \mathbf{X}, \mathbf{O}) = \nabla_{\xi} (-2 \text{lse}(\beta, (\mathbf{X} \parallel \mathbf{O})^T \xi) + \text{lse}(\beta, \mathbf{X}^T \xi) + \text{lse}(\beta, \mathbf{O}^T \xi)) \quad (71)$$

$$= -2 (\mathbf{X} \parallel \mathbf{O}) \text{softmax}(\beta (\mathbf{X} \parallel \mathbf{O})^T \xi) + \mathbf{X} \text{softmax}(\beta \mathbf{X}^T \xi) + \mathbf{O} \text{softmax}(\beta \mathbf{O}^T \xi) \quad (72)$$

When $\mathbf{X}_{\text{softmax}}(\beta \mathbf{X}^T \boldsymbol{\xi})$, $\mathbf{O}_{\text{softmax}}(\beta \mathbf{O}^T \boldsymbol{\xi})$, $\text{lse}(\beta, \mathbf{X}^T \boldsymbol{\xi})$ and $\text{lse}(\beta, \mathbf{O}^T \boldsymbol{\xi})$ are available, one can efficiently compute $(\mathbf{X} \parallel \mathbf{O})_{\text{softmax}}(\beta (\mathbf{X} \parallel \mathbf{O})^T \boldsymbol{\xi})$ as follows:

$$(\mathbf{X} \parallel \mathbf{O})_{\text{softmax}}(\beta (\mathbf{X} \parallel \mathbf{O})^T \boldsymbol{\xi}) \quad (73)$$

$$= \nabla_{\boldsymbol{\xi}} \text{lse}(\beta, (\mathbf{X} \parallel \mathbf{O})^T \boldsymbol{\xi}) \quad (74)$$

$$= \nabla_{\boldsymbol{\xi}} \beta^{-1} \log (\exp(\beta \text{lse}(\beta, \mathbf{X}^T \boldsymbol{\xi})) + \exp(\beta \text{lse}(\beta, \mathbf{O}^T \boldsymbol{\xi}))) \quad (75)$$

$$= (\mathbf{X}_{\text{softmax}}(\beta \mathbf{X}^T \boldsymbol{\xi}) \quad \mathbf{O}_{\text{softmax}}(\beta \mathbf{O}^T \boldsymbol{\xi}))_{\text{softmax}} \left(\beta \begin{pmatrix} \text{lse}(\beta, \mathbf{X}^T \boldsymbol{\xi}) \\ \text{lse}(\beta, \mathbf{O}^T \boldsymbol{\xi}) \end{pmatrix} \right) \quad (76)$$

We can also compute the gradient of $E_b(\boldsymbol{\xi}; \mathbf{X}, \mathbf{O})$ w.r.t. $\boldsymbol{\xi}$ via the log cosh-representation of E_b (see Equation (64)). The derivative of the log cosh function is

$$\frac{d}{dx} \beta^{-1} \log \cosh(\beta x) = \tanh(\beta x) \quad (77)$$

Therefore, we can compute the gradient of $E_b(\boldsymbol{\xi}; \mathbf{X}, \mathbf{O})$ as

$$\nabla_{\boldsymbol{\xi}} E_b(\boldsymbol{\xi}; \mathbf{X}, \mathbf{O}) \quad (78)$$

$$= \nabla_{\boldsymbol{\xi}} - 2\beta^{-1} \log \cosh \left(\frac{\beta}{2} (\text{lse}(\beta, \mathbf{O}^T \boldsymbol{\xi}) - \text{lse}(\beta, \mathbf{X}^T \boldsymbol{\xi})) \right) \quad (79)$$

$$= -\tanh \left(\frac{\beta}{2} (\text{lse}(\beta, \mathbf{O}^T \boldsymbol{\xi}) - \text{lse}(\beta, \mathbf{X}^T \boldsymbol{\xi})) \right) (\mathbf{O}_{\text{softmax}}(\beta \mathbf{O}^T \boldsymbol{\xi}) - \mathbf{X}_{\text{softmax}}(\beta \mathbf{X}^T \boldsymbol{\xi})) \quad (80)$$

$$= -\tanh \left(\frac{\beta}{2} (\text{lse}(\beta, \mathbf{X}^T \boldsymbol{\xi}) - \text{lse}(\beta, \mathbf{O}^T \boldsymbol{\xi})) \right) (\mathbf{X}_{\text{softmax}}(\beta \mathbf{X}^T \boldsymbol{\xi}) - \mathbf{O}_{\text{softmax}}(\beta \mathbf{O}^T \boldsymbol{\xi})) \quad (81)$$

Next, we would like to compute the gradient of $E_b(\boldsymbol{\xi}; \mathbf{X}, \mathbf{O})$ w.r.t. the memory matrices \mathbf{X} and \mathbf{O} . For this, let us first look at the gradient of the MHE $E(\boldsymbol{\xi}; \mathbf{X})$ w.r.t. a single stored pattern \mathbf{x}_i (where \mathbf{X} is the matrix of concatenated stored patterns $(\mathbf{x}_1, \mathbf{x}_2, \dots, \mathbf{x}_N)$):

$$\nabla_{\mathbf{x}_i} E(\boldsymbol{\xi}; \mathbf{X}) = -\boldsymbol{\xi}_{\text{softmax}}(\beta \mathbf{X}^T \boldsymbol{\xi})_i \quad (82)$$

Thus, the gradient w.r.t. the full memory matrix \mathbf{X} is

$$\nabla_{\mathbf{X}} E(\boldsymbol{\xi}; \mathbf{X}) = -\boldsymbol{\xi}_{\text{softmax}}(\beta \mathbf{X}^T \boldsymbol{\xi})^T \quad (83)$$

We can now also use the log cosh formulation of $E_b(\boldsymbol{\xi}; \mathbf{X}, \mathbf{O})$ to compute the gradient of $E_b(\boldsymbol{\xi}; \mathbf{X}, \mathbf{O})$, w.r.t \mathbf{X} and \mathbf{O} :

$$\nabla_{\mathbf{X}} E_b(\boldsymbol{\xi}; \mathbf{X}, \mathbf{O}) = \nabla_{\mathbf{X}} - 2\beta^{-1} \log \cosh \left(\frac{\beta}{2} (\text{lse}(\beta, \mathbf{X}^T \boldsymbol{\xi}) - \text{lse}(\beta, \mathbf{O}^T \boldsymbol{\xi})) \right) \quad (84)$$

$$= -\tanh \left(\frac{\beta}{2} (\text{lse}(\beta, \mathbf{X}^T \boldsymbol{\xi}) - \text{lse}(\beta, \mathbf{O}^T \boldsymbol{\xi})) \right) \boldsymbol{\xi}_{\text{softmax}}(\beta \mathbf{X}^T \boldsymbol{\xi})^T \quad (85)$$

$$(86)$$

Analogously, the gradient w.r.t \mathbf{O} is

$$\nabla_{\mathbf{O}} E_b(\boldsymbol{\xi}; \mathbf{X}, \mathbf{O}) = - \tanh \left(\frac{\beta}{2} (\text{lse}(\beta, \mathbf{O}^T \boldsymbol{\xi}) - \text{lse}(\beta, \mathbf{X}^T \boldsymbol{\xi})) \right) \boldsymbol{\xi}_{\text{softmax}(\beta \mathbf{O}^T \boldsymbol{\xi})}^T \quad (87)$$

G. Notes on the Relationship between Hopfield Boosting and other methods

G.1. Relation to Radial Basis Function Networks

This section shows the relation between radial basis function networks (RBF networks; [Moody & Darken, 1989](#)) and modern Hopfield energy (following [Schäfl et al., 2022](#)). Consider an RBF network with normalized linear weights:

$$\varphi(\boldsymbol{\xi}) = \sum_{i=1}^N \omega_i \exp\left(-\frac{\beta}{2} \|\boldsymbol{\xi} - \boldsymbol{\mu}_i\|_2^2\right) \quad (88)$$

where β denotes the inverse tied variance $\beta = \frac{1}{\sigma^2}$, and the ω_i are normalized using the softmax function:

$$\omega_i = \text{softmax}(\beta \mathbf{a})_i = \frac{\exp(\beta a_i)}{\sum_{j=1}^N \exp(\beta a_j)} \quad (89)$$

An energy can be obtained by taking the negative log of $\varphi(\boldsymbol{\xi})$:

$$E(\boldsymbol{\xi}) = -\beta^{-1} \log(\varphi(\boldsymbol{\xi})) \quad (90)$$

$$= -\beta^{-1} \log\left(\sum_{i=1}^N \omega_i \exp\left(-\frac{\beta}{2} \|\boldsymbol{\xi} - \boldsymbol{\mu}_i\|_2^2\right)\right) \quad (91)$$

$$= -\beta^{-1} \log\left(\sum_{i=1}^N \exp\left(\beta\left(-\frac{1}{2} \|\boldsymbol{\xi} - \boldsymbol{\mu}_i\|_2^2 + \beta^{-1} \log \text{softmax}(\beta \mathbf{a})_i\right)\right)\right) \quad (92)$$

$$= -\beta^{-1} \log\left(\sum_{i=1}^N \exp\left(\beta\left(-\frac{1}{2} \|\boldsymbol{\xi} - \boldsymbol{\mu}_i\|_2^2 + a_i - \text{lse}(\beta, \mathbf{a})\right)\right)\right) \quad (93)$$

$$= -\beta^{-1} \log\left(\sum_{i=1}^N \exp\left(\beta\left(-\frac{1}{2} \boldsymbol{\xi}^T \boldsymbol{\xi} + \boldsymbol{\mu}_i^T \boldsymbol{\xi} - \frac{1}{2} \boldsymbol{\mu}_i^T \boldsymbol{\mu}_i + a_i\right)\right)\right) + \text{lse}(\beta, \mathbf{a}) \quad (94)$$

Next, we define $a_i = \frac{1}{2} \boldsymbol{\mu}_i^T \boldsymbol{\mu}_i$

$$E(\boldsymbol{\xi}) = -\beta^{-1} \log\left(\sum_{i=1}^N \exp(\beta \boldsymbol{\mu}_i^T \boldsymbol{\xi})\right) + \frac{1}{2} \boldsymbol{\xi}^T \boldsymbol{\xi} + \text{lse}(\beta, \mathbf{a}) \quad (95)$$

Finally, we use the fact that $\text{lse}(\beta, \mathbf{a}) \leq \max_i a_i + \beta^{-1} \log N$

$$E(\boldsymbol{\xi}) = -\beta^{-1} \log\left(\sum_{i=1}^N \exp(\beta \boldsymbol{\mu}_i^T \boldsymbol{\xi})\right) + \frac{1}{2} \boldsymbol{\xi}^T \boldsymbol{\xi} + \beta^{-1} \log N + \frac{1}{2} M^2 \quad (96)$$

where $M = \max_i \|\boldsymbol{\mu}_i\|_2$

G.2. Contrastive Representation Learning

A commonly used loss function in contrastive representation learning (e.g., [Chen et al., 2020](#); [He et al., 2020](#)) is the InfoNCE loss ([Oord et al., 2018](#)):

$$\mathcal{L}_{\text{NCE}} = \mathbb{E}_{\substack{(x,y) \sim p_{\text{pos}} \\ \{x_i^-\}_{i=1}^M \sim p_{\text{data}}}} \left[-\log \frac{e^{f(x)^T f(y)/\tau}}{e^{f(x)^T f(y)/\tau} + \sum_i e^{f(x_i^-)^T f(y)/\tau}} \right] \quad (97)$$

Wang & Isola (2020) show that \mathcal{L}_{NCE} optimizes two objectives:

$$\mathcal{L}_{\text{NCE}} = \underbrace{\mathbb{E}_{(x,y) \sim p_{\text{pos}}} [-f(x)^T f(y)/\tau]}_{\text{Alignment}} + \underbrace{\mathbb{E}_{\substack{(x,y) \sim p_{\text{pos}} \\ \{x_i^-\}_{i=1}^M \sim p_{\text{data}}}} \left[\log \left(e^{f(x)^T f(y)/\tau} + \sum_i e^{f(x_i^-)^T f(x)/\tau} \right) \right]}_{\text{Uniformity}} \quad (98)$$

Alignment enforces that features from positive pairs are similar, while uniformity encourages a uniform distribution of the samples over the hypersphere.

In comparison, our proposed loss, \mathcal{L}_{OOD} , does not visibly enforce alignment between samples within the same class. Instead, we can observe that it promotes uniformity to the instances of the *foreign* class. Due to the constraints that are imposed by the geometry of the space the optimization is performed on, that is, $\|f(x)\| = 1$ when the samples move on a hypersphere, the loss encourages the patterns in the ID data have maximum distance to the samples of the AUX data, i.e., they concentrate on opposing poles of the hypersphere. A demonstration of this mechanism can be found in Appendix E.2 and E.3

G.3. Support Vector Machines

In the following, we will show the relation of Hopfield Boosting to support vector machines (SVMs; Cortes & Vapnik, 1995) with RBF kernel. We adopt and expand the arguments of Schäfl et al. (2022).

Assume we apply an SVM with RBF kernel to model the decision boundary between ID and AUX data. We train on the features $\mathbf{Z} = (\mathbf{x}_1, \dots, \mathbf{x}_N, \mathbf{o}_1, \dots, \mathbf{o}_M)$ and assume that the patterns are normalized, i.e., $\|\mathbf{x}_i\|_2 = 1$ and $\|\mathbf{o}_i\|_2 = 1$. We define the targets $(y_1, \dots, y_{(N+M)})$ as 1 for ID and -1 for AUX data. The decision rule of the SVM equates to

$$\hat{B}(\boldsymbol{\xi}) = \begin{cases} \text{ID} & \text{if } s(\boldsymbol{\xi}) \geq 0 \\ \text{OOD} & \text{if } s(\boldsymbol{\xi}) < 0 \end{cases} \quad (99)$$

where

$$s(\boldsymbol{\xi}) = \sum_{i=1}^{N+M} \alpha_i y_i k(\mathbf{z}_i, \boldsymbol{\xi}) \quad (100)$$

$$k(\mathbf{z}_i, \boldsymbol{\xi}) = \exp\left(-\frac{\beta}{2} \|\boldsymbol{\xi} - \mathbf{z}_i\|_2^2\right) \quad (101)$$

We assume that there is at least one support vector for both ID and AUX data, i.e., there exists at least one index i s.t. $\alpha_i y_i > 0$ and at least one index j s.t. $\alpha_j y_j < 0$. We now split the samples \mathbf{z}_i in $s(\boldsymbol{\xi})$ according to their label:

$$s(\boldsymbol{\xi}) = \sum_{i=1}^N \alpha_i k(\mathbf{x}_i, \boldsymbol{\xi}) - \sum_{i=1}^M \alpha_{N+i} k(\mathbf{o}_i, \boldsymbol{\xi}) \quad (102)$$

We define an alternative score:

$$s_{\text{frac}}(\boldsymbol{\xi}) = \frac{\sum_{i=1}^N \alpha_i k(\mathbf{x}_i, \boldsymbol{\xi})}{\sum_{i=1}^M \alpha_{N+i} k(\mathbf{o}_i, \boldsymbol{\xi})} \quad (103)$$

$$(104)$$

Because we assumed there is at least one support vector for both ID and AUX data and as the α_i are constrained to be non-negative and because $k(\cdot, \cdot) > 0$, the numerator and denominator are strictly positive. We can, therefore, specify a new decision rule $\hat{B}_{\text{frac}}(\boldsymbol{\xi})$.

$$\hat{B}_{\text{frac}}(\boldsymbol{\xi}) = \begin{cases} \text{ID} & \text{if } s_{\text{frac}}(\boldsymbol{\xi}) \geq 1 \\ \text{OOD} & \text{if } s_{\text{frac}}(\boldsymbol{\xi}) < 1 \end{cases} \quad (105)$$

Although the functions $s(\boldsymbol{\xi})$ and $s_{\text{frac}}(\boldsymbol{\xi})$ are different, the decision rules $\hat{B}(\boldsymbol{\xi})$ and $\hat{B}_{\text{frac}}(\boldsymbol{\xi})$ are equivalent. Another possible pair of score and decision rule is the following:

$$s_{\log}(\boldsymbol{\xi}) = \beta^{-1} \log(s_{\text{frac}}(\boldsymbol{\xi})) = \beta^{-1} \log \left(\sum_{i=1}^N \alpha_i k(\mathbf{x}_i, \boldsymbol{\xi}) \right) - \beta^{-1} \log \left(\sum_{i=1}^M \alpha_{N+i} k(\mathbf{o}_i, \boldsymbol{\xi}) \right) \quad (106)$$

$$\hat{B}_{\log}(\boldsymbol{\xi}) = \begin{cases} \text{ID} & \text{if } s_{\log}(\boldsymbol{\xi}) \geq 0 \\ \text{OOD} & \text{if } s_{\log}(\boldsymbol{\xi}) < 0 \end{cases} \quad (107)$$

Let us more closely examine the term $\beta^{-1} \log \left(\sum_{i=1}^N \alpha_i k(\mathbf{x}_i, \boldsymbol{\xi}) \right)$. We define $a_i = \beta^{-1} \log(\alpha_i)$.

$$\beta^{-1} \log \left(\sum_{i=1}^N \alpha_i k(\mathbf{x}_i, \boldsymbol{\xi}) \right) = \beta^{-1} \log \left(\sum_{i=1}^N \exp(\beta a_i) \exp \left(-\frac{\beta}{2} \|\boldsymbol{\xi} - \mathbf{x}_i\|_2^2 \right) \right) \quad (108)$$

$$= \beta^{-1} \log \left(\sum_{i=1}^N \exp(\beta a_i) \exp \left(-\frac{\beta}{2} \boldsymbol{\xi}^T \boldsymbol{\xi} + \beta \mathbf{x}_i^T \boldsymbol{\xi} - \frac{\beta}{2} \mathbf{x}_i^T \mathbf{x}_i \right) \right) \quad (109)$$

$$= \beta^{-1} \log \left(\sum_{i=1}^N \exp \left(-\frac{\beta}{2} \boldsymbol{\xi}^T \boldsymbol{\xi} + \beta \mathbf{x}_i^T \boldsymbol{\xi} - \frac{\beta}{2} \mathbf{x}_i^T \mathbf{x}_i + \beta a_i \right) \right) \quad (110)$$

$$= \beta^{-1} \log \left(\sum_{i=1}^N \exp(\beta \mathbf{x}_i^T \boldsymbol{\xi} + \beta a_i) \right) - \frac{1}{2} \boldsymbol{\xi}^T \boldsymbol{\xi} - \frac{1}{2} \quad (111)$$

We now construct a memory \mathbf{X}_H and query $\boldsymbol{\xi}_H$ such that we can compute (111) using the MHE (Equation (4)):

$$\mathbf{X}_H = \begin{pmatrix} \mathbf{x}_1 & \dots & \mathbf{x}_N \\ a_1 & \dots & a_N \end{pmatrix} \quad (112)$$

$$\boldsymbol{\xi}_H = \begin{pmatrix} \boldsymbol{\xi} \\ 1 \end{pmatrix} \quad (113)$$

We obtain

$$\mathbb{E}(\boldsymbol{\xi}_H; \mathbf{X}_H) = -\text{lse}(\beta, \mathbf{X}_H^T \boldsymbol{\xi}_H) + \frac{1}{2} \boldsymbol{\xi}_H^T \boldsymbol{\xi}_H + C \quad (114)$$

$$= -\beta^{-1} \log \left(\sum_{i=1}^N \exp(\beta \mathbf{x}_i^T \boldsymbol{\xi} + 1\beta a_i) \right) + \frac{1}{2} \boldsymbol{\xi}^T \boldsymbol{\xi} + \frac{1}{2} \cdot 1^2 + C \quad (115)$$

$$= -\beta^{-1} \log \left(\sum_{i=1}^N \exp(\beta \mathbf{x}_i^T \boldsymbol{\xi} + \beta a_i) \right) + \frac{1}{2} \boldsymbol{\xi}^T \boldsymbol{\xi} + \frac{1}{2} + C \quad (116)$$

$$= -\beta^{-1} \log \left(\sum_{i=1}^N \alpha_i k(\mathbf{x}_i, \boldsymbol{\xi}) \right) + C \quad (117)$$

We construct \mathbf{O}_H analogously to Equation (112) and thus can compute

$$s_{\log}(\boldsymbol{\xi}) = \mathbb{E}(\boldsymbol{\xi}_H; \mathbf{O}_H) - \mathbb{E}(\boldsymbol{\xi}_H; \mathbf{X}_H) = \text{lse}(\beta, \mathbf{X}_H^T \boldsymbol{\xi}_H) - \text{lse}(\beta, \mathbf{O}_H^T \boldsymbol{\xi}_H) \quad (118)$$

which is exactly the score Hopfield Boosting uses for determining whether a sample is OOD (Equation (9)). In contrast to SVMs, Hopfield Boosting uses a uniform weighting of the patterns in the memory when computing the score. However, Hopfield Boosting can emulate a weighting of the patterns by more frequently sampling patterns with high weights into the memory.

G.4. HE and SHE

Zhang et al. (2023a) introduce two post-hoc methods for OOD detection using MHE, which are called ‘‘Hopfield Energy’’ (HE) and ‘‘Simplified Hopfield Energy’’ (SHE). Like Hopfield Boosting, HE and SHE both employ the MHE to determine whether a sample is ID or OOD. However, unlike Hopfield Boosting, HE and SHE offer no possibility to include AUX data in the training process to improve the OOD detection performance of their method. The rest of this section is structured as follows: First, we briefly introduce the methods HE and SHE, second, we formally analyze the two methods, and third, we relate them to Hopfield Boosting.

Hopfield Energy (HE) The method HE (Zhang et al., 2023a) computes the OOD score $s_{\text{HE}}(\boldsymbol{\xi})$ as follows:

$$s_{\text{HE}}(\boldsymbol{\xi}) = \text{lse}(\beta, \mathbf{X}_c^T \boldsymbol{\xi}) \quad (119)$$

where $\mathbf{X}_c \in \mathbb{R}^{d \times N_c}$ denotes the memory $(\mathbf{x}_{c1}, \dots, \mathbf{x}_{cN_c})$ containing N_c encoded data instances of class c . HE uses the prediction of the ID classification head to determine which patterns to store in the Hopfield memory:

$$c = \underset{y}{\text{argmax}} p(y | \boldsymbol{\xi}^D) \quad (120)$$

Simplified Hopfield Energy (SHE) The method SHE (Zhang et al., 2023a) employs a simplified score $s_{\text{SHE}}(\boldsymbol{\xi})$:

$$s_{\text{SHE}}(\boldsymbol{\xi}) = \mathbf{m}_c^T \boldsymbol{\xi} \quad (121)$$

where $\mathbf{m}_c \in \mathbb{R}^d$ denotes the mean of the patterns in memory \mathbf{X}_c :

$$\mathbf{m}_c = \frac{1}{N_c} \sum_{i=1}^{N_c} \mathbf{x}_{ci} \quad (122)$$

Relation between HE and SHE In the following, we show a simple yet enlightening relation between the scores s_{HE} and s_{SHE} . For mathematical convenience, we first slightly modify the score s_{HE} :

$$s_{\text{HE}}(\boldsymbol{\xi}) = \text{lse}(\beta, \mathbf{X}_c^T \boldsymbol{\xi}) - \beta^{-1} \log N_c \quad (123)$$

All data sets which were employed in the experiments of Zhang et al. (2023a) (CIFAR-10 and CIFAR-100) are class-balanced. Therefore, the additional term $\beta^{-1} \log N_c$ does not change the result of the OOD detection on those data sets, as it only amounts to the same constant offset for all classes.

The function

$$\text{lse}(\beta, \mathbf{z}) - \beta^{-1} \log N = \beta^{-1} \log \left(\frac{1}{N} \sum_{i=1}^N \exp(\beta z_i) \right) \quad (124)$$

converges to the mean function as $\beta \rightarrow 0$:

$$\lim_{\beta \rightarrow 0} (\text{lse}(\beta, \mathbf{z}) - \beta^{-1} \log N) = \frac{1}{N} \sum_{i=1}^N z_i \quad (125)$$

We now investigate the behavior of s_{HE} in this limit:

$$\lim_{\beta \rightarrow 0} (\text{lse}(\beta, \mathbf{X}_c^T \boldsymbol{\xi}) - \beta^{-1} \log N) = \frac{1}{N} \sum_{i=1}^N (\mathbf{x}_{ci}^T \boldsymbol{\xi}) \quad (126)$$

$$= \left(\frac{1}{N} \sum_{i=1}^N \mathbf{x}_{ci} \right)^T \boldsymbol{\xi} \quad (127)$$

$$= \mathbf{m}_c^T \boldsymbol{\xi} \quad (128)$$

where

$$\mathbf{m}_c = \frac{1}{N} \sum_{i=1}^N \mathbf{x}_{ci} \quad (129)$$

Therefore, we have shown that

$$\lim_{\beta \rightarrow 0} s_{\text{HE}}(\boldsymbol{\xi}) = s_{\text{SHE}}(\boldsymbol{\xi}) \quad (130)$$

Relation of HE and SHE to Hopfield Boosting. In contrast to HE and SHE, Hopfield Boosting uses an AUX data set to learn a decision boundary between the ID and OOD regions during the training process. To do this, our work introduces a novel MHE-based energy function, $E_b(\boldsymbol{\xi}; \mathbf{X}, \mathcal{O})$, to determine how close a sample is to the learned decision boundary. Hopfield Boosting uses this energy function to frequently sample weak learners into the Hopfield memory and for computing a novel Hopfield-based OOD loss \mathcal{L}_{OOD} . To the best of our knowledge, we are the first to use MHE in this way to train a neural network.

The OOD detection score of Hopfield Boosting is

$$s(\xi) = \text{lse}(\beta, \mathbf{X}^T \xi) - \text{lse}(\beta, \mathbf{O}^T \xi). \quad (131)$$

where $\mathbf{X} \in \mathbb{R}^{d \times N}$ contains the full encoded training set $(\mathbf{x}_1, \dots, \mathbf{x}_N)$ of all classes and $\mathbf{O} \in \mathbb{R}^{d \times M}$ contains AUX samples. While certainly similar to s_{HE} , the Hopfield Boosting score s differs from s_{HE} in three crucial aspects:

1. Hopfield Boosting uses AUX data samples in the OOD detection score in order to create a sharper decision boundary between the ID and OOD regions.
2. Hopfield Boosting normalizes the patterns in the memories \mathbf{X} and \mathbf{O} and the query ξ to unit length, while HE and SHE use unnormalized patterns to construct their memories \mathbf{X}_c and their query pattern ξ .
3. The score of Hopfield Boosting, $s(\xi)$, contains the full encoded training data set, while s_{HE} only contains the patterns of a single class. Therefore Hopfield Boosting computes the similarities of a query sample ξ to the entire ID data set. In Appendix H.10, we show that this process only incurs a moderate overhead of 7.5% compared to the forward pass of the ResNet-18.

The selection of the score function $s(\xi)$ is only a small aspect of Hopfield Boosting. Hopfield Boosting additionally samples informative AUX data close to the decision boundary, optimizes an MHE-based loss function, and thereby learns a sharp decision boundary between ID and OOD regions. Those three aspects are novel contributions of Hopfield Boosting. In contrast, the work of [Zhang et al. \(2023a\)](#) solely focuses on the selection of a suitable Hopfield-based OOD detection score for post-hoc OOD detection.

Table 2: OOD detection performance on CIFAR-10. We compare results from Hopfield Boosting, DOS (Jiang et al., 2024), DOE (Wang et al., 2023b), DivOE (Zhu et al., 2023), DAL (Wang et al., 2023a), MixOE (Zhang et al., 2023b), POEM (Ming et al., 2022), EBO-OE (Liu et al., 2020), and MSP-OE (Hendrycks et al., 2019b) on ResNet-18. \downarrow indicates “lower is better” and \uparrow “higher is better”. All values in %. Standard deviations are estimated across five training runs.

OOD Dataset	Metric	HB (ours)	DOS	DOE	DivOE	DAL	MixOE	POEM	EBO-OE	MSP-OE
SVHN	FPR95 \downarrow	0.23\pm0.08	3.09 \pm 0.75	1.97 \pm 0.58	6.21 \pm 0.84	1.25 \pm 0.62	27.54 \pm 2.46	1.48 \pm 0.68	2.66 \pm 0.91	4.31 \pm 1.10
	AUROC \uparrow	99.57\pm0.06	99.15 \pm 0.22	99.60\pm0.13	98.53 \pm 0.08	99.61\pm0.15	95.37 \pm 0.44	99.33 \pm 0.15	99.15 \pm 0.23	99.20 \pm 0.15
LSUN-Crop	FPR95 \downarrow	0.82 \pm 0.17	3.66 \pm 0.98	3.22 \pm 0.45	1.88 \pm 0.25	4.17 \pm 0.27	0.14\pm0.07	4.02 \pm 0.91	6.82 \pm 0.74	7.02 \pm 1.14
	AUROC \uparrow	99.40 \pm 0.04	99.04 \pm 0.20	99.30 \pm 0.12	99.50 \pm 0.02	99.13 \pm 0.02	99.61\pm0.11	98.89 \pm 0.15	98.43 \pm 0.10	98.83 \pm 0.15
LSUN-Resize	FPR95 \downarrow	0.00\pm0.00	0.00 \pm 0.00	0.00\pm0.00	0.00\pm0.00	0.00\pm0.00	0.16 \pm 0.17	0.00\pm0.00	0.00\pm0.00	0.00\pm0.00
	AUROC \uparrow	99.98 \pm 0.02	99.99 \pm 0.01	100.00\pm0.00	99.89 \pm 0.05	99.92 \pm 0.05	99.89 \pm 0.06	99.88 \pm 0.12	99.98 \pm 0.02	99.96 \pm 0.00
Textures	FPR95 \downarrow	0.16\pm0.02	1.28 \pm 0.20	2.75 \pm 0.57	1.20 \pm 0.11	0.95 \pm 0.13	4.68 \pm 0.22	0.49 \pm 0.04	1.11 \pm 0.17	2.29 \pm 0.16
	AUROC \uparrow	99.84\pm0.01	99.63 \pm 0.04	99.35 \pm 0.12	99.59 \pm 0.02	99.74 \pm 0.01	98.91 \pm 0.07	99.72 \pm 0.05	99.61 \pm 0.02	99.57 \pm 0.01
iSUN	FPR95 \downarrow	0.00\pm0.00	0.00\pm0.00	0.00\pm0.00	0.00\pm0.00	0.00\pm0.00	0.17 \pm 0.12	0.00\pm0.00	0.00\pm0.00	0.00\pm0.00
	AUROC \uparrow	99.97 \pm 0.02	99.99 \pm 0.01	100.00\pm0.00	99.88 \pm 0.05	99.93 \pm 0.04	99.87 \pm 0.05	99.87 \pm 0.12	99.98 \pm 0.01	99.96 \pm 0.00
Places 365	FPR95 \downarrow	4.28\pm0.23	12.26 \pm 0.97	19.72 \pm 2.39	13.70 \pm 0.50	14.22 \pm 0.51	16.30 \pm 1.09	7.70 \pm 0.68	11.77 \pm 0.68	21.42 \pm 0.88
	AUROC \uparrow	98.51\pm0.10	96.63 \pm 0.43	95.06 \pm 0.72	96.95 \pm 0.09	96.77 \pm 0.07	96.92 \pm 0.22	97.56 \pm 0.26	96.39 \pm 0.30	95.91 \pm 0.17
Mean	FPR95 \downarrow	0.92	3.38	4.61	3.83	3.43	8.17	2.28	3.73	5.84
	AUROC \uparrow	99.55	99.07	98.88	99.06	99.18	98.43	99.21	98.92	98.90

H. Additional Experiments & Experimental Details

H.1. Hyperparameter Setup

Like Yang et al. (2022), we use SGD with an initial learning rate of 0.1 and a weight decay of $5 \cdot 10^{-4}$. We decrease the learning rate during the training process with a cosine schedule (Loshchilov & Hutter, 2016). We sample mini-batches of size 128 per data set. For a fair comparison, we apply these settings to all OOD detection methods that we test. For training Hopfield Boosting, we use a single value for β throughout the training and evaluation process and for all OOD data sets. We tune the value of β for each ID data set separately by selecting the value of β from the set $\{2, 4, 8, 16, 32\}$ that performs best in the validation process. We select λ — the weight for the OOD loss \mathcal{L}_{OOD} — from $\{0.1, 0.25, 0.5, 1.0\}$. In our experiments, $\beta = 4$ and $\lambda = 0.5$ yields the best results for CIFAR-10 and CIFAR-100. For ImageNet-1K, we set $\beta = 32$ and $\lambda = 0.25$. To tune the hyperparameters, we use a validation process with different OOD data for model selection. Specifically, we validate the model on MNIST (LeCun et al., 1998), and ImageNet-RC with different pre-processing than in training (resize to 32x32 pixels instead of crop to 32x32 pixels), as well as Gaussian and uniform noise. We conducted our experiments on various NVIDIA GPUs (e.g., Titan V, A100) on an internal cluster.

H.2. Results on CIFAR-10

Table 2 shows the results from Section 4 with five additional baselines.

H.3. Results on CIFAR-100

We conduct experiments on CIFAR-100 as ID data set. In this setting, we closely follow the experimental setup for CIFAR-10 described in Section 4.2. Table 3 shows that Hopfield Boosting surpasses POEM (the previously best method), improving the mean FPR95 from 11.76 to 7.95. On the SVHN data set, Hopfield Boosting improves the FPR95 metric the most, decreasing it from 33.59 to 13.27.

H.4. Results on ImageNet-1K

Following Wang et al. (2023b), we evaluate Hopfield Boosting on the large-scale benchmark: We use ImageNet-1K (Russakovsky et al., 2015) as ID data set and ImageNet-21K (Ridnik et al., 2021) as AUX data set. The OOD test data sets are Textures (Cimpoi et al., 2014), SUN (Xu et al., 2015), Places 365 (López-Cifuentes et al., 2020), and iNaturalist (Van Horn et al., 2018). In this setting, we fine-tune a pre-trained ResNet-50 using Hopfield Boosting. As we show in Table 4, Hopfield Boosting surpasses all methods in our comparison in terms of both mean FPR95 and mean AUROC. Compared to POEM (the previously best method) Hopfield Boosting improves the mean FPR95 from 50.74 to 36.60. This demonstrates that Hopfield Boosting scales very favourably to large-scale settings.

Table 3: OOD detection performance on CIFAR-100. We compare results from Hopfield Boosting, DOS (Jiang et al., 2024), DOE (Wang et al., 2023b), DivOE (Zhu et al., 2023), DAL (Wang et al., 2023a), MixOE (Zhang et al., 2023b), POEM (Ming et al., 2022), EBO-OE (Liu et al., 2020), and MSP-OE (Hendrycks et al., 2019b) on ResNet-18. ↓ indicates “lower is better” and ↑ “higher is better”. All values in %. Standard deviations are estimated across five training runs.

OOD Dataset	Metric	HB (ours)	DOS	DOE	DivOE	DAL	MixOE	POEM	EBO-OE	MSP-OE
SVHN	FPR95 ↓	13.27 ^{±5.46}	9.84^{±2.75}	19.38 ^{±4.60}	28.77 ^{±5.42}	19.95 ^{±2.34}	41.54 ^{±13.16}	33.59 ^{±4.12}	36.33 ^{±2.95}	19.86 ^{±6.90}
	AUROC ↑	97.07 ^{±0.81}	97.64^{±0.39}	95.72 ^{±1.12}	94.25 ^{±0.98}	95.69 ^{±0.66}	92.27 ^{±2.71}	94.06 ^{±0.51}	92.93 ^{±0.72}	95.74 ^{±1.60}
LSUN-Crop	FPR95 ↓	12.68^{±2.38}	19.40 ^{±2.45}	28.23 ^{±2.69}	35.10 ^{±4.23}	24.24 ^{±2.12}	23.10 ^{±7.39}	15.72 ^{±3.46}	21.06 ^{±3.12}	32.88 ^{±1.28}
	AUROC ↑	96.54^{±0.65}	96.42^{±0.35}	93.79 ^{±0.88}	92.45 ^{±0.94}	95.04 ^{±0.43}	96.11 ^{±1.09}	96.85^{±0.60}	95.79 ^{±0.62}	92.85 ^{±0.33}
LSUN-Resize	FPR95 ↓	0.00^{±0.00}	0.01 ^{±0.00}	0.05 ^{±0.04}	0.01 ^{±0.00}	0.00^{±0.00}	10.27 ^{±10.72}	0.00^{±0.00}	0.00^{±0.00}	0.03 ^{±0.01}
	AUROC ↑	99.98 ^{±0.01}	99.96 ^{±0.02}	99.99 ^{±0.01}	99.99^{±0.00}	99.94 ^{±0.02}	97.99 ^{±1.92}	99.57 ^{±0.09}	99.57 ^{±0.03}	99.97 ^{±0.00}
Textures	FPR95 ↓	2.35^{±0.13}	6.02 ^{±0.52}	19.42 ^{±1.58}	11.52 ^{±0.49}	5.22 ^{±0.39}	28.99 ^{±6.79}	2.89 ^{±0.32}	5.07 ^{±0.54}	10.34 ^{±0.40}
	AUROC ↑	99.22^{±0.02}	98.33 ^{±0.11}	94.93 ^{±0.48}	97.02 ^{±0.08}	98.50 ^{±0.16}	94.24 ^{±1.21}	98.97 ^{±0.08}	98.15 ^{±0.16}	97.42 ^{±0.08}
iSUN	FPR95 ↓	0.00^{±0.00}	0.03 ^{±0.01}	0.01 ^{±0.02}	0.06 ^{±0.01}	0.01 ^{±0.02}	14.40 ^{±13.48}	0.00^{±0.00}	0.00^{±0.00}	0.08 ^{±0.02}
	AUROC ↑	99.98 ^{±0.01}	99.95 ^{±0.02}	99.99^{±0.00}	99.97 ^{±0.00}	99.93 ^{±0.02}	97.23 ^{±2.59}	99.59 ^{±0.09}	99.57 ^{±0.03}	99.96 ^{±0.01}
Places 365	FPR95 ↓	19.36 ^{±1.02}	32.13 ^{±1.55}	58.68 ^{±4.15}	44.20 ^{±0.95}	33.43 ^{±1.11}	47.01 ^{±6.41}	18.39^{±0.68}	26.68 ^{±2.18}	45.96 ^{±0.85}
	AUROC ↑	95.85^{±0.37}	91.73 ^{±0.39}	83.47 ^{±1.55}	88.28 ^{±0.26}	91.10 ^{±0.29}	89.20 ^{±1.86}	95.03 ^{±0.71}	91.35 ^{±0.70}	87.77 ^{±0.15}
Mean	FPR95 ↓	7.94	11.24	20.96	19.94	13.81	27.55	11.76	14.86	18.19
	AUROC ↑	98.11	97.34	94.65	95.33	96.70	94.51	97.34	96.23	95.62

Table 4: OOD detection performance on ImageNet-1K. We compare results from Hopfield Boosting, DOS (Jiang et al., 2024), DOE (Wang et al., 2023b), DivOE (Zhu et al., 2023), DAL (Wang et al., 2023a), MixOE (Zhang et al., 2023b), POEM (Ming et al., 2022), EBO-OE (Liu et al., 2020), and MSP-OE (Hendrycks et al., 2019b) on ResNet-50. ↓ indicates “lower is better” and ↑ “higher is better”. All values in %. Standard deviations are estimated across five training runs.

		HB (ours)	DOS	DOE	DivOE	DAL	MixOE	POEM	EBO-OE	MSP-OE
Textures	FPR95 ↓	44.59 ^{±1.05}	40.29 ^{±0.93}	83.83 ^{±7.19}	42.80 ^{±0.74}	43.88 ^{±0.66}	41.05 ^{±4.91}	31.26 ^{±0.67}	29.67^{±1.26}	48.38 ^{±0.87}
	AUROC ↑	88.01 ^{±0.57}	89.88 ^{±0.18}	64.22 ^{±9.25}	88.18 ^{±0.06}	87.39 ^{±0.15}	88.51 ^{±1.29}	92.22^{±0.14}	92.40^{±0.23}	86.25 ^{±0.25}
SUN	FPR95 ↓	37.37^{±1.84}	59.29 ^{±0.96}	83.73 ^{±8.78}	61.00 ^{±0.57}	65.31 ^{±0.61}	65.14 ^{±2.53}	57.46 ^{±0.90}	57.69 ^{±1.61}	66.01 ^{±0.26}
	AUROC ↑	91.24^{±0.52}	84.30 ^{±0.21}	72.95 ^{±7.94}	83.64 ^{±0.30}	81.47 ^{±0.22}	82.20 ^{±0.72}	85.38 ^{±0.35}	85.83 ^{±0.60}	81.45 ^{±0.20}
Places 365	FPR95 ↓	53.31^{±2.05}	69.72 ^{±1.01}	86.30 ^{±6.69}	71.09 ^{±0.60}	74.46 ^{±0.75}	71.34 ^{±1.49}	68.87 ^{±1.05}	70.03 ^{±1.83}	74.58 ^{±0.44}
	AUROC ↑	87.10^{±0.52}	81.62 ^{±0.22}	70.37 ^{±7.17}	80.35 ^{±0.33}	78.72 ^{±0.28}	80.31 ^{±0.42}	81.79 ^{±0.40}	81.35 ^{±0.63}	78.89 ^{±0.19}
iNaturalist	FPR95 ↓	11.11^{±0.66}	49.55 ^{±1.41}	70.82 ^{±13.89}	30.51 ^{±0.42}	51.92 ^{±0.74}	47.28 ^{±1.55}	45.37 ^{±1.79}	49.02 ^{±4.40}	51.73 ^{±1.35}
	AUROC ↑	97.65^{±0.20}	90.49 ^{±0.38}	83.82 ^{±5.75}	93.81 ^{±0.10}	88.33 ^{±0.21}	90.19 ^{±0.35}	92.01 ^{±0.33}	91.44 ^{±0.79}	88.51 ^{±0.30}
Mean	FPR95 ↓	36.60	54.71	81.17	51.35	58.90	56.20	50.74	51.60	60.17
	AUROC ↑	91.00	86.57	72.84	86.49	83.98	85.30	87.85	87.75	83.78

H.5. Comparison HE/SHE

Since Hopfield Boosting shares similarities with the MHE-based methods HE and SHE (Zhang et al., 2023a), we also looked at the approach as used for their methods. We use the same ResNet-18 as a backbone network as we used in the experiments for Hopfield Boosting, but train it on CIFAR-10 without OE. We modify the approach of Zhang et al. (2023a) to not only use the penultimate layer, but perform a search over all layer activation combinations of the backbone for the best-performing combination. We also do not use the classifier to separate by class. From the search, we see that the concatenated activations of layers 3 and 5 give the best performance on average, so we use this setting. We experience a quite noticeable drop in performance compared to their results (Table 5). Since the computation of the MHE is the same, we assume the reason for the performance drop is the different training of the ResNet-18 backbone network, where (Zhang et al., 2023a) used strong augmentations.

H.6. Ablations

In the first ablation we look at the impact of the boosting itself, specifically the sampling of weak learners. The comparison is done by training the same network architecture (Resnet-18) with and without weak learner sampling. The experiment shows that boosting has a noticeable effect on the performance: Hopfield Boosting performs better with weak learner sampling.

We investigate the impact of different encoder backbone architectures on OOD detection performance with Hopfield Boosting. The baseline uses a ResNet-18 as the encoder architecture. For the ablation, the following architectures are

Table 5: Comparison between HE, SHE and our version. ↓ indicates “lower is better” and ↑ indicates “higher is better”.

OOD Dataset	Ours		HE		SHE	
	FPR95 ↓	AUROC ↑	FPR95 ↓	AUROC ↑	FPR95 ↓	AUROC ↑
SVHN	36.79	93.18	35.81	92.35	35.07	92.81
LSUN-Crop	13.10	97.25	17.74	95.96	18.19	96.10
LSUN-Resize	16.65	96.84	20.69	95.87	21.66	95.85
Textures	44.54	89.38	46.29	86.67	46.19	87.44
iSUN	19.20	96.08	22.52	95.08	23.25	95.06
Places 365	39.02	90.63	41.56	88.41	42.57	88.38
Mean	28.21	93.89	30.77	92.39	31.66	92.60

Table 6: OOD detection performance on CIFAR-10. We compare Hopfield Boosting trained with weighted sampling and random sampling on ResNet-18. ↓ indicates “lower is better” and ↑ indicates “higher is better”. All values in %. Standard deviations are estimated across five training runs.

OOD Dataset	Weighted Sampling		Random Sampling	
	FPR95 ↓	AUROC ↑	FPR95 ↓	AUROC ↑
SVHN	0.23\pm0.08	99.57\pm0.06	0.70 \pm 0.13	99.55\pm0.08
LSUN-Crop	0.82\pm0.20	99.40\pm0.05	1.58 \pm 0.31	99.24 \pm 0.10
LSUN-Resize	0.00\pm0.00	99.98\pm0.02	0.00\pm0.00	99.98\pm0.01
Textures	0.16\pm0.02	99.85\pm0.01	0.26 \pm 0.06	99.81 \pm 0.02
iSUN	0.00\pm0.00	99.97 \pm 0.02	0.00\pm0.00	99.99\pm0.00
Places 365	4.28\pm0.26	98.51\pm0.11	6.20 \pm 0.21	97.68 \pm 0.21
Mean	0.92	99.55	1.46	99.38

used as a comparison: ResNet-34, ResNet-50, and Densenet-100. It can be observed, that the larger architectures lead to a slight increase in OOD performance (Table 7). We also see that a change in architecture from ResNet to Densenet leads to a different OOD behavior: The result on the Places365 data set is greatly improved, while the performance on SVHN is noticeably worse than on the ResNet architectures. The FPR95 of Densenet on SVHN also shows a high variance, which is due to one of the five independent training runs performing very badly at detecting SVHN samples as OOD: The worst run scores an FPR95 5.59, while the best run achieves an FPR95 of 0.24.

H.7. Effect on Learned Representation

In order to analyze the impact of Hopfield Boosting on learned representations, we utilize the output of our model’s embedding layer (see 4.2) as the input for a manifold learning-based visualization. Uniform Manifold Approximation and Projection (UMAP) [McInnes et al. \(2018\)](#) is a non-linear dimensionality reduction technique known for its ability to preserve both global and local structure in high-dimensional data.

First, we train two models – with and without Hopfield Boosting – and extract the embeddings of both ID and OOD data sets from them. This results in a 512-dimensional vector representation for each data point, which we further reduce to two dimensions with UMAP. The training data for UMAP always corresponds to the training data of the respective method. That is, the model trained without Hopfield Boosting is solely trained on CIFAR-10 data, and the model trained with Hopfield Boosting is presented with CIFAR-10 and AUX data during training, respectively. We then compare the learned representations concerning ID and OOD data.

Figure 8 shows the UMAP embeddings of ID (CIFAR-10) and OOD (AUX and SVHN) data based on our model trained without (a) and with Hopfield Boosting (b). Without Hopfield Boosting, OOD data points typically overlap with ID data points, with just a few exceptions, making it difficult to differentiate between them. Conversely, Hopfield Boosting allows to distinctly separate ID and OOD data in the embedding.

Table 7: Comparison of OOD detection performance on CIFAR-10 of Hopfield Boosting on different encoders. \downarrow indicates “lower is better” and \uparrow indicates “higher is better”. Standard deviations are estimated across five independent training runs.

OOD Dataset	ResNet-18		ResNet-34		ResNet-50		Densenet-100	
	FPR95 \downarrow	AUROC \uparrow	FPR95 \downarrow	AUROC \uparrow	FPR95 \downarrow	AUROC \uparrow	FPR95 \downarrow	AUROC \uparrow
SVHN	0.23 \pm 0.08	99.57 \pm 0.06	0.33 \pm 0.25	99.63 \pm 0.07	0.19\pm0.09	99.64\pm0.11	2.11 \pm 2.76	99.31 \pm 0.35
LSUN-Crop	0.82 \pm 0.20	99.40 \pm 0.05	0.65 \pm 0.14	99.54 \pm 0.07	0.69 \pm 0.15	99.47 \pm 0.09	0.40\pm0.23	99.52\pm0.09
LSUN-Resize	0.00\pm0.00	99.98 \pm 0.02	0.00\pm0.00	99.89 \pm 0.04	0.00\pm0.00	99.93 \pm 0.10	0.00\pm0.00	100.0\pm0.00
Textures	0.16 \pm 0.02	99.85 \pm 0.01	0.15 \pm 0.07	99.89 \pm 0.04	0.16 \pm 0.07	99.83 \pm 0.01	0.08\pm0.03	99.88\pm0.01
iSUN	0.00\pm0.00	99.97 \pm 0.02	0.00\pm0.00	99.98 \pm 0.02	0.00\pm0.00	99.98 \pm 0.02	0.00\pm0.00	99.99\pm0.01
Places 365	4.28 \pm 0.26	98.51 \pm 0.11	4.13 \pm 0.54	98.46 \pm 0.22	4.75 \pm 0.45	98.71 \pm 0.05	2.56\pm0.20	99.26\pm0.03
Mean	0.92	99.55	0.88	99.57	0.97	99.59	0.86	99.66

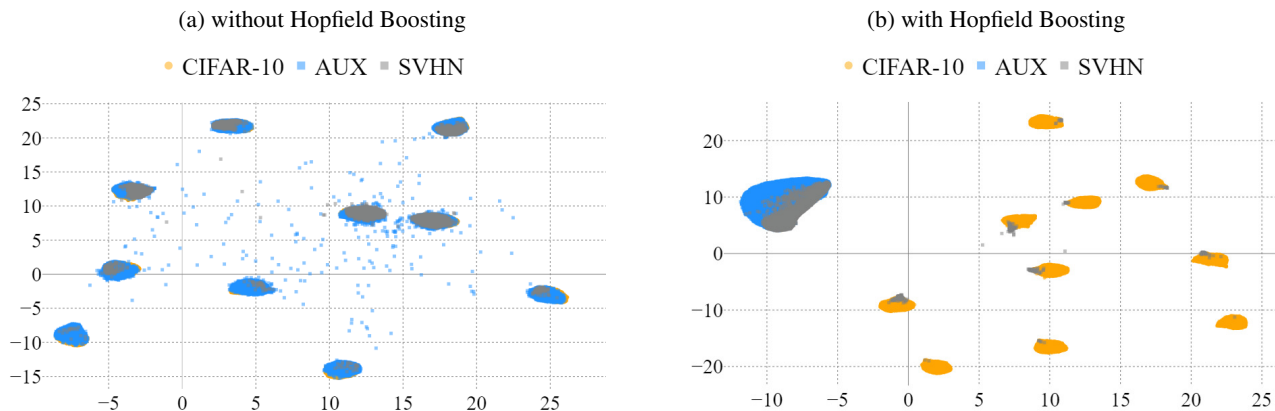


Figure 8: UMAP embeddings of ID (CIFAR-10) and OOD (AUX and SVHN) data based on our model trained without (a) and with Hopfield Boosting (b). Clearly, without Hopfield Boosting, the embedded OOD data points tend to overlap with the ID data points, making it impossible to distinguish between ID and OOD. On the other hand, Hopfield Boosting shows a clear separation of ID and OOD data in the embedding.

H.8. OOD Examples from the Places 365 Data Set with High Semantic Similarity to CIFAR-10

We observe that Hopfield Boosting and all competing methods struggle with correctly classifying the samples from the Places 365 data set as OOD the most. Table 1 shows that for Hopfield Boosting, the FPR95 for the Places 365 data set with CIFAR-10 as the ID data set is at 4.28. The second worst FPR95 for Hopfield Boosting was measured on the LSUN-Crop data set at 0.82.

We inspect the 100 images from Places 365 that perform worst (i.e., that achieve the highest score $s(\xi)$) on a model trained with Hopfield Boosting on the CIFAR-10 data set as the in-distribution data set. Figure 9 shows that within those 100 images, the Places 365 data set contains a non-negligible amount of data instances that show objects from semantic classes contained in CIFAR-10 (e.g., horses, automobiles, dogs, trucks, and airplanes). We argue that data instances that clearly show objects of semantic classes contained in CIFAR-10 should be considered as in-distribution, which Hopfield Boosting correctly recognizes. Therefore, a certain amount of error can be anticipated on the Places 365 data set for all OOD detection methods. We leave a closer evaluation of the amount of the anticipated error up to future work.

For comparison, Figure 10 shows the 100 images from Places 365 with the lowest score $s(\xi)$, as evaluated by a model trained with Hopfield Boosting on CIFAR-10. There are no objects visible that have clear semantic overlap with the CIFAR-10 classes.

Energy-based Hopfield Boosting for Out-of-Distribution Detection

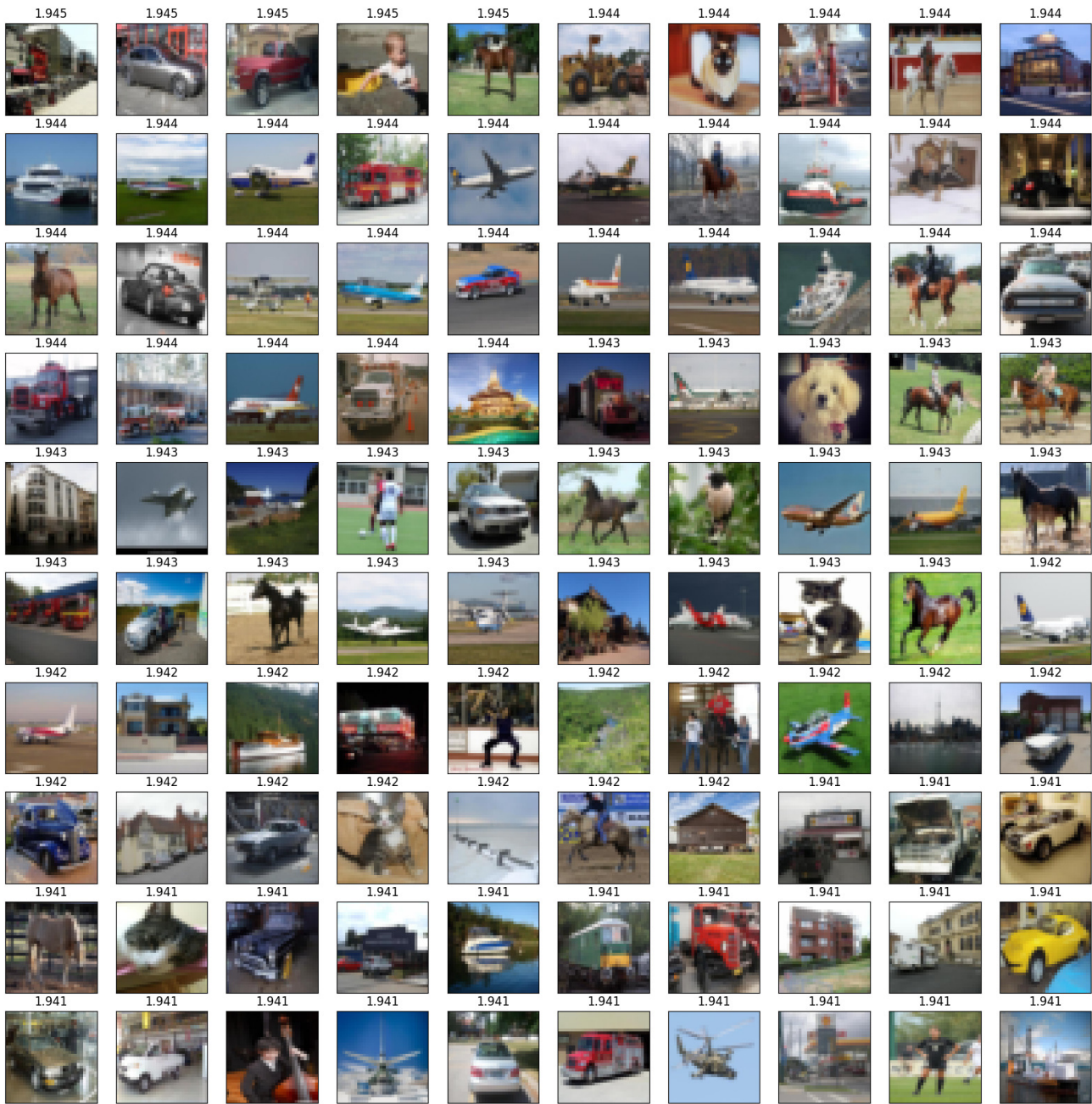


Figure 9: The set of top-100 images from the Places 365 data set which Hopfield Boosting recognized as in-distribution. The image captions show $s(\xi)$ of the respective image below the caption.

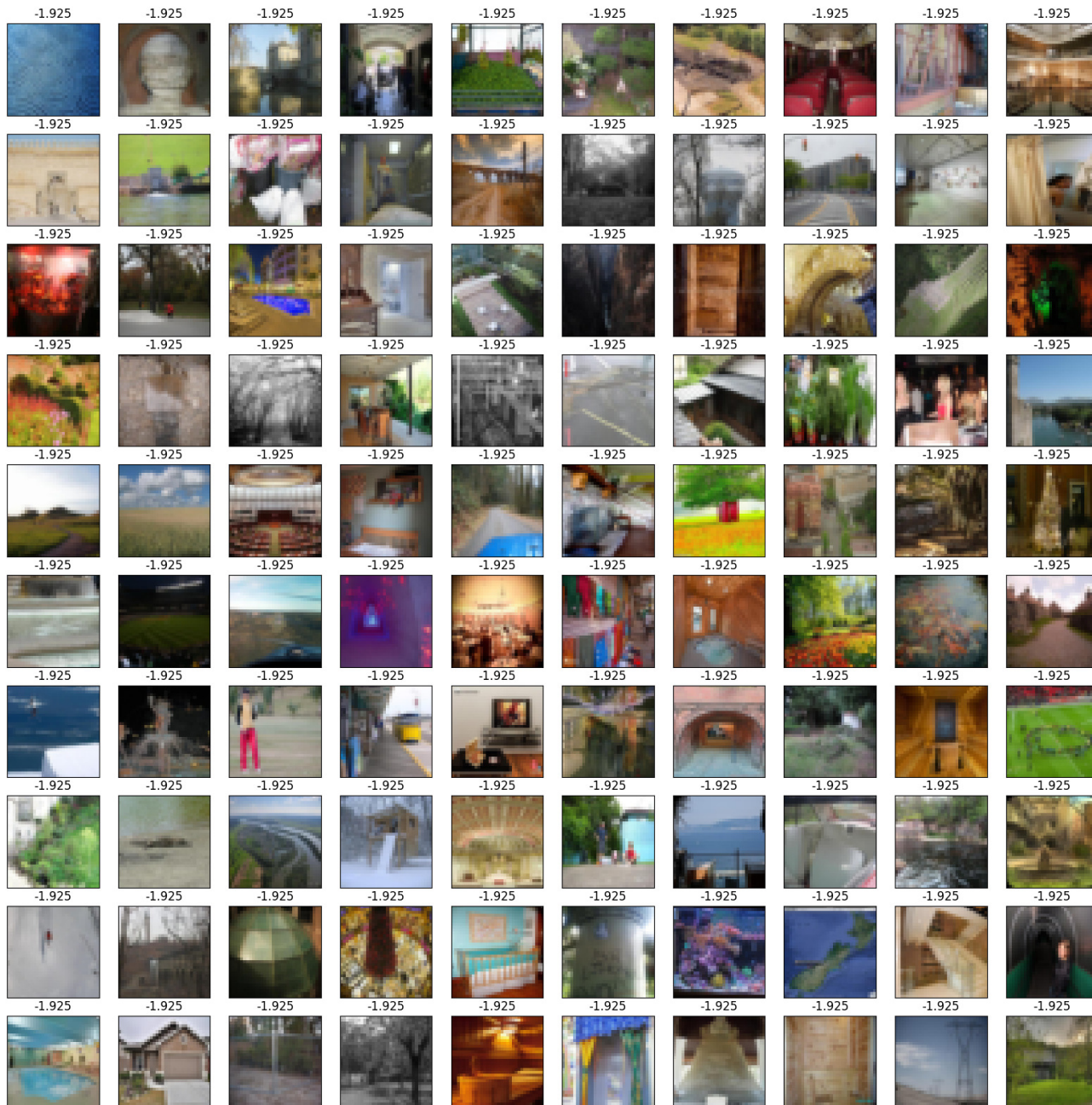


Figure 10: The set of top-100 images from the Places 365 data set which Hopfield Boosting recognized as out-of-distribution. The image captions show $s(\xi)$ of the respective image below the caption.

H.9. Results on Noticeably Different Data Sets

The choice of additional data sets should not be driven by a desire to showcase good performance; rather, we suggest opting for data that highlights weaknesses, as it holds the potential to drive investigations and uncover novel insights. Simple toy data is preferable due to its typically clearer and more intuitive characteristics compared to complex natural image data. In alignment with these considerations, the following data sets captivated our interest: iCartoonFace (Zheng et al., 2020), Four Shapes (smeschke, 2018), and Retail Product Checkout (RPC) (Wei et al., 2022). In Figure 11, we show random samples from these data sets to demonstrate the noticeable differences compared to CIFAR-10.

Table 8: Comparison between EBO-OE (Liu et al., 2020) and our version. \downarrow indicates “lower is better” and \uparrow indicates “higher is better”.

OOD Dataset	Hopfield Boosting		EBO-OE	
	FPR95 \downarrow	AUROC \uparrow	FPR95 \downarrow	AUROC \uparrow
iCartoonFace	0.60	99.57	4.01	98.94
Four Shapes	40.81	90.53	62.55	75.34
RPC	4.07	98.65	18.51	96.10

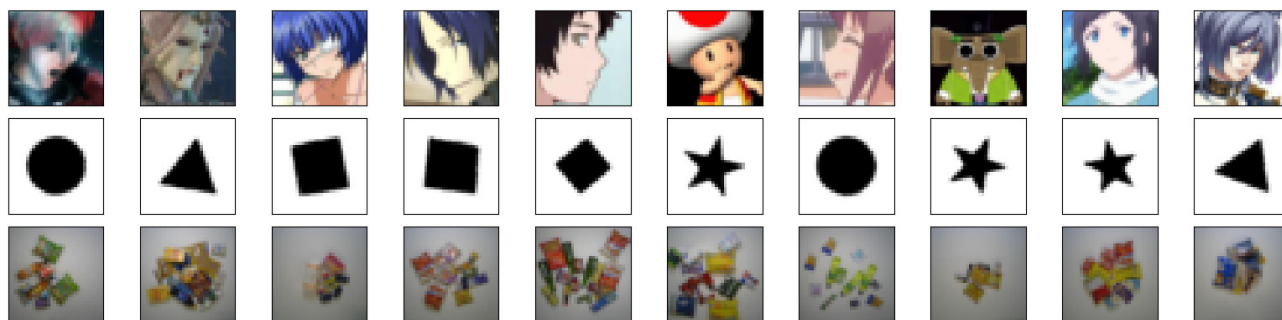


Figure 11: Random samples from three data sets, each noticeably different from CIFAR-10. First row: iCartoonFace; Second row: Four shapes; Third row: RPC.

In Table 8, we present some preliminary results using models trained with the respective method on CIFAR-10 as ID data set (as in Table 1). Results for comparison are presented for EBO-OE only, as time constraints prevented experimenting with additional baseline methods. Although one would expect near-perfect results due to the evident disparities with CIFAR-10, Four Shapes (smeschke, 2018) and RPC (Wei et al., 2022) seem to defy that expectation. Their results indicate a weakness in the capability to identify outliers robustly since many samples are classified as inliers. Only iCartoonFace (Zheng et al., 2020) is correctly detected as OOD, at least to a large degree. Interestingly, the weakness uncovered by this data is present in both methods, although more pronounced in EBO-OE. Therefore, we suspect that this specific behavior may be a general weakness when training OOD detectors using OE, an aspect we plan to investigate further in our future work.

H.10. Runtime Considerations for Inference

When using Hopfield Boosting in inference, an additional inference step is needed to check whether a given sample is ID or OOD. Namely, to obtain the score (Equation (9)) of a query sample ξ^D , Hopfield Boosting computes the dot product similarity of the embedding obtained from $\xi = \phi(\xi^D)$ to all samples in the Hopfield memories \mathbf{X} and \mathbf{O} . In our experiments, \mathbf{X} contains the full in-distribution data set (50,000 samples) and \mathbf{O} contains a subset of the AUX data set of equal size. We investigate the computational overhead of computing the dot-product similarity to 100,000 samples in relation to the computational load of the encoder. For this, we feed 100 batches of size 1024 to an encoder (1) without using the score and (2) with using the score, measure the runtimes per batch, and compute the mean and standard deviation. We conduct this experiment with four different encoders on an NVIDIA Titan V GPU. The results are shown in Figure 12 and Table 9. One can see that, especially for larger models, the computational overhead of determining the score is very moderate in comparison.

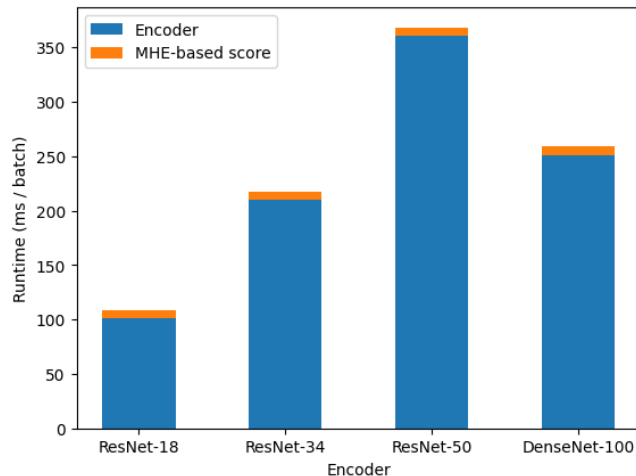


Figure 12: Mean inference runtimes for Hopfield Boosting on four different encoders on an NVIDIA Titan V GPU. We plot the contributions to the total runtime of the encoder and the MHE-based score (Equation (9)) separately. The evaluation shows that the score computation adds a negligible amount of computational overhead to the total runtime.

Table 9: Inference runtimes for Hopfield Boosting with four different encoders on an NVIDIA Titan V GPU. We compare the runtime of the encoder only and the runtime of the encoder with the MHE-based score computation (Equation (9)) combined.

Encoder	Time encoder (ms / batch)	Time encoder + score (ms / batch)	Rel. overhead (%)
ResNet-18	100.93 ± 0.24	108.50 ± 0.19	7.50
ResNet-34	209.80 ± 0.40	217.33 ± 0.51	3.59
ResNet-50	360.93 ± 1.51	368.17 ± 0.62	2.01
Densenet-100	251.24 ± 1.36	258.82 ± 0.84	3.02

H.11. Compute Resources

Our experiments were conducted on an internal cluster equipped with a variety of different GPU types (ranging from the NVIDIA Titan V to the NVIDIA A100-SXM-80GB). For our experiments on ImageNet-1K, we additionally used resources of an external cluster that is equipped with NVIDIA A100-SXM-64GB GPUs.

For our experiments with Hopfield Boosting on CIFAR-10 and CIFAR-100, one run (100 epochs) of Hopfield Boosting trained for about 8.0 hours on a single NVIDIA RTX 2080 Ti GPU and required 4.3 GB of VRAM. Finding the hyperparameters required 160h of compute for CIFAR-10 and CIFAR-100, respectively. These were divided across four RTX 2080 Ti. Estimating the standard deviation required 40 hours of compute on a single RTX 2080 Ti for CIFAR-10 and CIFAR-100 respectively.

For ImageNet-1K, one run (4 epochs) of Hopfield Boosting trained for about 4.4 hours on a single NVIDIA A-100-SXM64GB GPU and required 26.9 GB of VRAM. Finding the optimal hyperparameters required a total of 86h of compute, divided across 20 NVIDIA A-100-SXM64GB GPUs. Estimating the standard deviation required 22 hours of compute, divided across 5 NVIDIA A-100-SXM64GB GPUs.

The amount of resources reported above cover the compute for obtaining the results of Hopfield Boosting reported in the paper. The total amount of compute resources for the project is substantially higher. Notable additional compute expenses are preliminary training runs during the development of Hopfield Boosting, and the training runs for tuning the hyperparameters and evaluating the results of the methods we compare Hopfield Boosting to.

H.12. Data Sets and Licenses

We provide a list of the data sets we used in our experiments and, where applicable, specify their licenses:

- CIFAR-10 ([Krizhevsky, 2009](#)): License unknown
- CIFAR-100 ([Krizhevsky, 2009](#)): License unknown
- ImageNet-RC ([Chrabaszcz et al., 2017](#)): Custom License²
- SVHN ([Netzer et al., 2011](#)): Creative Commons (CC)
- Textures ([Cimpoi et al., 2014](#)): Custom License³
- iSUN ([Xu et al., 2015](#)): License unknown
- Places 365 ([López-Cifuentes et al., 2020](#)): License unknown
- LSUN ([Yu et al., 2015](#)): License unknown
- ImageNet-1K ([Russakovsky et al., 2015](#)): Custom License²
- ImageNet-21K ([Ridnik et al., 2021](#)): Custom License²
- SUN ([Isola et al., 2011](#)): License unknown
- iNaturalist ([Van Horn et al., 2018](#)): Custom License⁴

²<https://image-net.org/download.php>

³<https://www.robots.ox.ac.uk/~vgg/data/dtd/index.html>

⁴https://github.com/visipedia/inat_comp/tree/master/2017

Table 10: OOD detection performance on CIFAR-10. We compare results from Hopfield Boosting, PALM (Lu et al., 2024), NPOS (Tao et al., 2023), SSD+ (Schwag et al., 2021), ASH (Djurisic et al., 2023), GEN (Liu et al., 2023), EBO (Liu et al., 2020), MaxLogit (Hendrycks et al., 2019a), and MSP (Hendrycks & Gimpel, 2017) on ResNet-18. ↓ indicates “lower is better” and ↑ “higher is better”. All values in %. Standard deviations are estimated across five training runs.

		HB (ours)	PALM	NPOS	SSD+	ASH	GEN	EBO	MaxLogit	MSP
SVHN	FPR95 ↓	0.23 ^{±0.08}	1.24 ^{±0.49}	9.04 ^{±1.13}	3.05 ^{±0.22}	25.17 ^{±9.55}	33.26 ^{±5.99}	32.10 ^{±6.41}	33.27 ^{±6.18}	49.41 ^{±3.77}
	AUROC ↑	99.57 ^{±0.06}	99.70 ^{±0.12}	98.37 ^{±0.23}	99.41 ^{±0.06}	94.86 ^{±2.09}	93.53 ^{±1.42}	93.43 ^{±1.60}	93.29 ^{±1.57}	92.48 ^{±0.93}
LSUN-Crop	FPR95 ↓	0.82 ^{±0.17}	1.21 ^{±0.27}	5.52 ^{±0.50}	2.83 ^{±1.10}	13.13 ^{±1.81}	19.40 ^{±2.22}	17.25 ^{±2.30}	18.50 ^{±2.24}	38.32 ^{±2.61}
	AUROC ↑	99.40 ^{±0.04}	99.65 ^{±0.05}	98.97 ^{±0.04}	99.37 ^{±0.16}	97.33 ^{±0.36}	96.48 ^{±0.46}	96.73 ^{±0.46}	96.52 ^{±0.47}	94.37 ^{±0.53}
LSUN-Resize	FPR95 ↓	0.00 ^{±0.00}	27.01 ^{±5.82}	26.85 ^{±3.14}	34.30 ^{±2.17}	38.18 ^{±5.78}	31.50 ^{±3.92}	30.69 ^{±4.03}	31.64 ^{±4.01}	45.82 ^{±3.48}
	AUROC ↑	99.98 ^{±0.02}	95.41 ^{±0.74}	95.68 ^{±0.36}	94.78 ^{±0.25}	90.39 ^{±2.00}	94.04 ^{±0.84}	94.02 ^{±0.86}	93.90 ^{±0.86}	92.84 ^{±0.80}
Textures	FPR95 ↓	0.16 ^{±0.02}	17.32 ^{±2.50}	27.72 ^{±2.55}	21.20 ^{±2.20}	46.08 ^{±6.22}	44.62 ^{±4.14}	44.67 ^{±4.46}	44.97 ^{±4.44}	55.04 ^{±2.86}
	AUROC ↑	99.84 ^{±0.01}	96.82 ^{±0.71}	95.36 ^{±0.35}	96.46 ^{±0.35}	88.32 ^{±2.08}	90.12 ^{±1.32}	89.61 ^{±1.50}	89.56 ^{±1.48}	90.10 ^{±0.92}
iSUN	FPR95 ↓	0.00 ^{±0.00}	25.71 ^{±4.83}	26.90 ^{±3.52}	35.71 ^{±2.27}	42.41 ^{±6.28}	35.85 ^{±4.05}	34.99 ^{±4.33}	36.02 ^{±4.18}	49.10 ^{±3.06}
	AUROC ↑	99.97 ^{±0.02}	95.60 ^{±0.65}	95.74 ^{±0.38}	94.49 ^{±0.25}	89.06 ^{±2.26}	93.05 ^{±0.84}	92.99 ^{±0.90}	92.88 ^{±0.90}	91.99 ^{±0.74}
Places 365	FPR95 ↓	4.28 ^{±0.23}	22.97 ^{±2.17}	32.62 ^{±0.13}	24.99 ^{±1.21}	48.03 ^{±2.04}	45.82 ^{±1.07}	44.87 ^{±1.11}	45.63 ^{±1.26}	57.58 ^{±0.97}
	AUROC ↑	98.51 ^{±0.10}	94.95 ^{±0.53}	93.76 ^{±0.12}	94.93 ^{±0.22}	85.65 ^{±0.77}	88.68 ^{±0.28}	88.53 ^{±0.30}	88.42 ^{±0.29}	88.06 ^{±0.25}
Mean	FPR95 ↓	0.92	15.91	21.44	20.35	35.50	35.07	34.09	35.00	49.21
	AUROC ↑	99.55	97.02	96.31	96.57	90.94	92.65	92.55	92.43	91.64
Method type		OE	Training	Training	Training	Post-hoc	Post-hoc	Post-hoc	Post-hoc	Post-hoc
Augmentations		Weak	Strong	Strong	Strong	Weak	Weak	Weak	Weak	Weak
Auxiliary outlier data		✓	✗	✗	✗	✗	✗	✗	✗	✗

H.13. Non-OE Baselines

To confirm the prevailing notion that OE methods can improve the OOD detection capability in general, we compare Hopfield Boosting to 3 training methods (Schwag et al., 2021; Tao et al., 2023; Lu et al., 2024) and 5 post-hoc methods (Hendrycks & Gimpel, 2017; Hendrycks et al., 2019b; Liu et al., 2020, 2023; Djurisic et al., 2023). For all methods, we train a ResNet-18 on CIFAR-10. For Hopfield Boosting, we use the same training setup as described in section 4.2. For the post-hoc methods, we do not use the auxiliary outlier data. For the training methods, we use the training procedures described in the respective publications for 100 epochs. Notably, all training methods employ stronger augmentations than the OE or the post-hoc methods. The OE and post-hoc methods use the following augmentations (denoted as “Weak”):

1. RandomCrop (32x32), padding 4
2. RandomHorizontalFlip

The training methods use the following augmentations (denoted as “Strong”):

1. RandomResizedCrop (32x32), scale 0.2-1
2. RandomHorizontalFlip
3. ColorJitter applied with probability 0.8
4. RandomGrayscale applied with probability 0.2

Table 10 shows the results of the comparison of Hopfield Boosting to the post-hoc and training methods. Hopfield Boosting is better at OOD detection than all non-OE baselines on CIFAR-10 in terms of both mean AUROC and mean FPR95 by a large margin. Further, Hopfield Boosting achieves the best OOD detection on all OOD data sets in terms of FPR95 and AUROC, except for SVHN and LSUN-Crop, where PALM (Lu et al., 2024) shows better AUROC results. An interesting avenue for future work is to combine one of the non-OE based training methods with the OE method Hopfield Boosting.

I. Informativeness of Sampling with High Boundary Scores

This section adopts and expands the arguments of [Ming et al. \(2022\)](#) on sampling with high boundary scores.

We assume the extracted features of a trained deep neural network to approximately equal a Gaussian mixture model with equal class priors:

$$p(\boldsymbol{\xi}) = \frac{1}{2}\mathcal{N}(\boldsymbol{\xi}; \boldsymbol{\mu}, \sigma^2\mathbf{I}) + \frac{1}{2}\mathcal{N}(\boldsymbol{\xi}; -\boldsymbol{\mu}, \sigma^2\mathbf{I}) \quad (132)$$

$$p_{\text{ID}}(\boldsymbol{\xi}) = p(\boldsymbol{\xi}|\text{ID}) = \mathcal{N}(\boldsymbol{\xi}; \boldsymbol{\mu}, \sigma^2\mathbf{I}) \quad (133)$$

$$p_{\text{AUX}}(\boldsymbol{\xi}) = p(\boldsymbol{\xi}|\text{AUX}) = \mathcal{N}(\boldsymbol{\xi}; -\boldsymbol{\mu}, \sigma^2\mathbf{I}) \quad (134)$$

Using the MHE and sufficient data from those distributions, we can estimate the densities $p(\boldsymbol{\xi})$, $p(\boldsymbol{\xi}|\text{ID})$ and $p(\boldsymbol{\xi}|\text{AUX})$.

Lemma I.1. (see Lemma E.1 in [Ming et al. \(2022\)](#)) Assume the M sampled data points $\mathbf{o}_i \sim p_{\text{AUX}}$ satisfy the following constraint on high boundary scores $E_b(\boldsymbol{\xi})$

$$\frac{-\sum_{i=1}^M E_b(\mathbf{o}_i)}{M} \leq \epsilon \quad (135)$$

Then they have

$$\sum_{i=1}^M |2\boldsymbol{\mu}^T \mathbf{o}_i| \leq M\epsilon\sigma^2 \quad (136)$$

Proof. They first obtain the expression for $E_b(\boldsymbol{\xi})$ under the Gaussian mixture model described above and can express $p(\text{AUX}|\boldsymbol{\xi})$ as

$$p(\text{AUX}|\boldsymbol{\xi}) = \frac{p(\boldsymbol{\xi}|\text{AUX})p(\text{AUX})}{p(\boldsymbol{\xi})} \quad (137)$$

$$= \frac{\frac{1}{2}p(\boldsymbol{\xi}|\text{AUX})}{\frac{1}{2}p(\boldsymbol{\xi}|\text{ID}) + \frac{1}{2}p(\boldsymbol{\xi}|\text{AUX})} \quad (138)$$

$$= \frac{(2\pi\sigma^2)^{-d/2} \exp(-\frac{1}{2\sigma^2}\|\boldsymbol{\xi} - \boldsymbol{\mu}\|_2^2)}{(2\pi\sigma^2)^{-d/2} \exp(-\frac{1}{2\sigma^2}\|\boldsymbol{\xi} + \boldsymbol{\mu}\|_2^2) + (2\pi\sigma^2)^{-d/2} \exp(-\frac{1}{2\sigma^2}\|\boldsymbol{\xi} - \boldsymbol{\mu}\|_2^2)} \quad (139)$$

$$= \frac{1}{1 + \exp(-\frac{1}{2\sigma^2}(\|\boldsymbol{\xi} - \boldsymbol{\mu}\|_2^2 - \|\boldsymbol{\xi} + \boldsymbol{\mu}\|_2^2))} \quad (140)$$

When defining $f_{\text{AUX}}(\boldsymbol{\xi}) = \frac{1}{2\sigma^2}(\|\boldsymbol{\xi} - \boldsymbol{\mu}\|_2^2 - \|\boldsymbol{\xi} + \boldsymbol{\mu}\|_2^2)$ such that $p(\text{AUX}|\boldsymbol{\xi}) = \sigma(f_{\text{AUX}}(\boldsymbol{\xi})) = \frac{1}{1 + \exp(-f_{\text{AUX}}(\boldsymbol{\xi}))}$, they define E_b as follows:

$$E_b(\boldsymbol{\xi}) = -|f_{\text{AUX}}(\boldsymbol{\xi})| \quad (141)$$

$$= -\frac{1}{2\sigma^2} |\|\boldsymbol{\xi} - \boldsymbol{\mu}\|_2^2 - \|\boldsymbol{\xi} + \boldsymbol{\mu}\|_2^2| \quad (142)$$

$$= -\frac{1}{2\sigma^2} |\boldsymbol{\xi}^T \boldsymbol{\xi} - 2\boldsymbol{\mu}^T \boldsymbol{\xi} + \boldsymbol{\mu}^T \boldsymbol{\mu} - (\boldsymbol{\xi}^T \boldsymbol{\xi} + 2\boldsymbol{\mu}^T \boldsymbol{\xi} + \boldsymbol{\mu}^T \boldsymbol{\mu})| \quad (143)$$

$$= -\frac{|2\boldsymbol{\mu}^T \boldsymbol{\xi}|}{\sigma^2} \quad (144)$$

Therefore, the constraint in Equation (136) is translated to

$$\sum_{i=1}^M |2\boldsymbol{\mu}^T \mathbf{o}_i| \leq M\epsilon\sigma^2 \quad (145)$$

□

As $\max_{i \in M} |\boldsymbol{\mu}^T \mathbf{o}_i| \leq \sum_{i=1}^M |\boldsymbol{\mu}^T \mathbf{o}_i|$ given a fixed M , the selected samples can be seen as generated from p_{AUX} with the constraint that all samples lie within the two hyperplanes in Equation (145).

Parameter estimation. Now they show the benefit of such constraint in controlling the sample complexity. Assume the signal/noise ratio is large: $\frac{\|\boldsymbol{\mu}\|}{\sigma} = r \gg 1$, and $\epsilon \leq 1$ is some constant.

Assume the classifier is given by

$$\boldsymbol{\theta} = \frac{1}{N+M} \left(\sum_{i=1}^M \mathbf{x}_i - \sum_{i=1}^N \mathbf{o}_i \right) \quad (146)$$

where $\mathbf{o}_i \sim p_{\text{AUX}}$ and $\mathbf{x}_i \sim p_{\text{ID}}$. One can decompose $\boldsymbol{\theta}$. Assuming $M = N$:

$$\boldsymbol{\theta} = \boldsymbol{\mu} + \frac{1}{2}\boldsymbol{\eta} + \frac{1}{2}\boldsymbol{\omega} \quad (147)$$

$$\boldsymbol{\eta} = \frac{1}{N} \left(\sum_{i=1}^N \mathbf{x}_i \right) - \boldsymbol{\mu} \quad (148)$$

$$\boldsymbol{\omega} = \frac{1}{N} \left(\sum_{i=1}^M -\mathbf{o}_i \right) - \boldsymbol{\mu} \quad (149)$$

We would now like to determine the distributions of the random variables $\|\boldsymbol{\eta}\|_2^2$ and $\boldsymbol{\mu}^T \boldsymbol{\eta}$

$$\|\boldsymbol{\eta}\|_2^2 = \sum_{i=1}^d \eta_i^2 \quad (150)$$

$$\eta_i \sim \mathcal{N}\left(0, \frac{\sigma^2}{N}\right) \quad (151)$$

$$\frac{\sqrt{N}}{\sigma} \eta_i \sim \mathcal{N}(0, 1) \quad (152)$$

$$\left(\frac{\sqrt{N}}{\sigma} \eta_i\right)^2 \sim \chi_1^2 \quad (153)$$

Therefore, for $\|\boldsymbol{\eta}\|_2^2$ we have

$$\frac{N}{\sigma^2} \|\boldsymbol{\eta}\|_2^2 = \sum_{i=1}^d \left(\frac{\sqrt{N}}{\sigma} \eta_i\right)^2 \sim \chi_d^2 \quad (154)$$

Now we would like to determine the distribution of $\boldsymbol{\mu}^T \boldsymbol{\eta}$:

$$\boldsymbol{\mu}^T \boldsymbol{\eta} = \sum_{i=1}^d \mu_i \eta_i \quad (155)$$

$$\mu_i \eta_i \sim \mathcal{N}\left(0, \frac{\sigma^2 \mu_i^2}{N}\right) \quad (156)$$

$$\sum_{i=1}^d \mu_i \eta_i \sim \mathcal{N}\left(0, \sum_{i=1}^d \frac{\sigma^2 \mu_i^2}{N}\right) \quad (157)$$

$$\sum_{i=1}^d \mu_i \eta_i \sim \mathcal{N}\left(0, \frac{\sigma^2}{N} \sum_{i=1}^d \mu_i^2\right) \quad (158)$$

$$\frac{\boldsymbol{\mu}^T \boldsymbol{\eta}}{\|\boldsymbol{\mu}\|} \sim \mathcal{N}\left(0, \frac{\sigma^2}{N}\right) \quad (159)$$

Concentration bounds. They now develop concentration bounds for $\|\boldsymbol{\eta}\|_2^2$ and $\boldsymbol{\mu}^T \boldsymbol{\eta}$. First, we look at $\|\boldsymbol{\eta}\|_2^2$. A concentration bound for χ_d^2 is:

$$\mathbb{P}(X - d \geq 2\sqrt{dx} + 2x) \leq \exp(-x) \quad (160)$$

By assuming $x = \frac{d}{8\sigma^2}$ we obtain

$$\mathbb{P}(X - d \geq 2\sqrt{d \frac{d}{8\sigma^2}} + 2 \frac{d}{8\sigma^2}) \leq \exp\left(-\frac{d}{8\sigma^2}\right) \quad (161)$$

$$\mathbb{P}\left(X \geq \frac{d}{\sqrt{2}\sigma} + \frac{d}{4\sigma^2} + d\right) \leq \exp\left(-\frac{d}{8\sigma^2}\right) \quad (162)$$

$$\mathbb{P}\left(\frac{N}{\sigma^2} \|\boldsymbol{\eta}\|_2^2 \geq \frac{d}{\sqrt{2}\sigma} + \frac{d}{4\sigma^2} + d\right) \leq \exp\left(-\frac{d}{8\sigma^2}\right) \quad (163)$$

$$\mathbb{P}(\|\boldsymbol{\eta}\|_2^2 \geq \frac{\sigma^2}{N} \left(\frac{d}{\sqrt{2}\sigma} + \frac{d}{4\sigma^2} + d\right)) \leq \exp\left(-\frac{d}{8\sigma^2}\right) \quad (164)$$

If $d \geq 2$ we have that⁵

$$\frac{d}{\sqrt{2}\sigma} + \frac{d}{4\sigma^2} > \frac{1}{\sigma} \quad (165)$$

and thus, the above bound can be simplified when assuming $d \geq 2$ as follows:

$$\mathbb{P}(\|\boldsymbol{\eta}\|_2^2 \geq \frac{\sigma^2}{N} \left(\frac{1}{\sigma} + d\right)) \leq \exp\left(-\frac{d}{8\sigma^2}\right) \quad (166)$$

For $\|\boldsymbol{\omega}\|_2^2$, since all \mathbf{o}_i is drawn i.i.d. from p_{AUX} , under the constraint in Equation (145), the distribution of $\boldsymbol{\omega}$ can be seen as a truncated distribution of $\boldsymbol{\eta}$. Thus, with some finite positive constant c , we have

$$\mathbb{P}(\|\boldsymbol{\omega}\|_2^2 \geq \frac{\sigma^2}{N} \left(d + \frac{1}{\sigma}\right)) \leq c \mathbb{P}(\|\boldsymbol{\eta}\|_2^2 \geq \frac{\sigma^2}{N} \left(d + \frac{1}{\sigma}\right)) \leq c \exp\left(-\frac{d}{8\sigma^2}\right) \quad (167)$$

⁵Strictly, the bound is valid for $d > \sqrt{2}$

Now, we develop a bound for $\boldsymbol{\mu}^T \boldsymbol{\eta}$. A concentration bound for $\mathcal{N}(\mu, \sigma^2)$ is

$$\mathbb{P}(X - \mu \geq t) \leq \exp\left(\frac{-t^2}{2\sigma^2}\right) \quad (168)$$

By applying $\frac{\boldsymbol{\mu}^T \boldsymbol{\eta}}{\|\boldsymbol{\mu}\|} \sim \mathcal{N}(0, \frac{\sigma^2}{N})$ to the above bound we obtain

$$\mathbb{P}\left(\frac{\boldsymbol{\mu}^T \boldsymbol{\eta}}{\|\boldsymbol{\mu}\|} \geq t\right) \leq \exp\left(\frac{-t^2 N}{2\sigma^2}\right) \quad (169)$$

Assuming $t = (\sigma\|\boldsymbol{\mu}\|)^{1/2}$ we obtain

$$\mathbb{P}\left(\frac{\boldsymbol{\mu}^T \boldsymbol{\eta}}{\|\boldsymbol{\mu}\|} \geq (\sigma\|\boldsymbol{\mu}\|)^{1/2}\right) \leq \exp\left(\frac{-(\sigma\|\boldsymbol{\mu}\|)N}{2\sigma^2}\right) \quad (170)$$

$$\mathbb{P}\left(\frac{\boldsymbol{\mu}^T \boldsymbol{\eta}}{\|\boldsymbol{\mu}\|} \geq (\sigma\|\boldsymbol{\mu}\|)^{1/2}\right) \leq \exp\left(\frac{-\|\boldsymbol{\mu}\|N}{2\sigma}\right) \quad (171)$$

Due to symmetry, we have

$$\mathbb{P}\left(-\frac{\boldsymbol{\mu}^T \boldsymbol{\eta}}{\|\boldsymbol{\mu}\|} \leq -(\sigma\|\boldsymbol{\mu}\|)^{1/2}\right) \leq \exp\left(\frac{-\|\boldsymbol{\mu}\|N}{2\sigma}\right) \quad (172)$$

$$\mathbb{P}\left(-\frac{\boldsymbol{\mu}^T \boldsymbol{\eta}}{\|\boldsymbol{\mu}\|} \leq -(\sigma\|\boldsymbol{\mu}\|)^{1/2}\right) + \mathbb{P}\left(\frac{\boldsymbol{\mu}^T \boldsymbol{\eta}}{\|\boldsymbol{\mu}\|} \geq (\sigma\|\boldsymbol{\mu}\|)^{1/2}\right) \leq 2 \exp\left(\frac{-\|\boldsymbol{\mu}\|N}{2\sigma}\right) \quad (173)$$

We can rewrite the above bound using the absolute value function.

$$\mathbb{P}\left(\left|\frac{\boldsymbol{\mu}^T \boldsymbol{\eta}}{\|\boldsymbol{\mu}\|}\right| \geq (\sigma\|\boldsymbol{\mu}\|)^{1/2}\right) \leq 2 \exp\left(\frac{-\|\boldsymbol{\mu}\|N}{2\sigma}\right) \quad (174)$$

Benefit of high boundary scores. We will now show why sampling with high boundary scores is beneficial. Recall the results from Equations (145) and (149):

$$\sum_{i=1}^M |2\boldsymbol{\mu}^T \boldsymbol{o}_i| \leq M\epsilon\sigma^2 \quad (175)$$

$$\boldsymbol{\omega} = \frac{1}{M} \left(-\sum_{i=1}^M \boldsymbol{o}_i\right) - \boldsymbol{\mu} \quad (176)$$

The triangle inequality is

$$|a + b| \leq |a| + |b| \quad (177)$$

$$|a + (-b)| \leq |a| + |b| \quad (178)$$

Using the two facts above and the triangle inequality we can bound $|\boldsymbol{\mu}^T \boldsymbol{\omega}|$:

$$\frac{1}{M} \left| \sum_{i=1}^M \boldsymbol{\mu}^T \boldsymbol{o}_i \right| \leq \frac{\sigma^2 \epsilon}{2} \quad (179)$$

$$\frac{1}{M} \left| - \sum_{i=1}^M \boldsymbol{\mu}^T \boldsymbol{o}_i \right| \leq \frac{\sigma^2 \epsilon}{2} \quad (180)$$

$$\frac{1}{M} \left| - \sum_{i=1}^M \boldsymbol{\mu}^T \boldsymbol{o}_i \right| + \|\boldsymbol{\mu}\|_2^2 \leq \frac{\sigma^2 \epsilon}{2} + \|\boldsymbol{\mu}\|_2^2 \quad (181)$$

$$\frac{1}{M} \left| - \sum_{i=1}^M \boldsymbol{\mu}^T \boldsymbol{o}_i - \boldsymbol{\mu}^T \boldsymbol{\mu} \right| \leq \frac{\sigma^2 \epsilon}{2} + \|\boldsymbol{\mu}\|_2^2 \quad (182)$$

$$|\boldsymbol{\mu}^T \boldsymbol{\omega}| \leq \|\boldsymbol{\mu}\|_2^2 + \frac{\sigma^2 \epsilon}{2} \quad (183)$$

Developing a lower bound. Let

$$\|\boldsymbol{\eta}\|_2^2 \leq \frac{\sigma^2}{N} \left(d + \frac{1}{\sigma} \right) \quad (184)$$

$$\|\boldsymbol{\omega}\|_2^2 \leq \frac{\sigma^2}{N} \left(d + \frac{1}{\sigma} \right) \quad (185)$$

$$\frac{|\boldsymbol{\mu}^T \boldsymbol{\eta}|}{\|\boldsymbol{\mu}\|} \leq (\sigma \|\boldsymbol{\mu}\|)^{1/2} \quad (186)$$

hold simultaneously. The probability of this happening can be bounded as follows: We define T and its complement \bar{T} :

$$T = \left\{ \|\boldsymbol{\eta}\|_2^2 \leq \frac{\sigma^2}{N} \left(d + \frac{1}{\sigma} \right) \right\} \cap \left\{ \|\boldsymbol{\omega}\|_2^2 \leq \frac{\sigma^2}{N} \left(d + \frac{1}{\sigma} \right) \right\} \cap \left\{ \frac{|\boldsymbol{\mu}^T \boldsymbol{\eta}|}{\|\boldsymbol{\mu}\|} \leq (\sigma \|\boldsymbol{\mu}\|)^{1/2} \right\} \quad (187)$$

$$\bar{T} = \left\{ \|\boldsymbol{\eta}\|_2^2 > \frac{\sigma^2}{N} \left(d + \frac{1}{\sigma} \right) \right\} \cup \left\{ \|\boldsymbol{\omega}\|_2^2 > \frac{\sigma^2}{N} \left(d + \frac{1}{\sigma} \right) \right\} \cup \left\{ \frac{|\boldsymbol{\mu}^T \boldsymbol{\eta}|}{\|\boldsymbol{\mu}\|} > (\sigma \|\boldsymbol{\mu}\|)^{1/2} \right\} \quad (188)$$

With $\mathbb{P}(T) + \mathbb{P}(\bar{T}) = 1$. The probability $\mathbb{P}(\bar{T})$ can be bounded using Boole's inequality and the results in Equations (166), (167) and (174):

$$\mathbb{P}(\bar{T}) \leq \exp(-d/8\sigma^2) + c \exp(-d/8\sigma^2) + 2 \exp\left(-\frac{\|\boldsymbol{\mu}\|N}{2\sigma}\right) \quad (189)$$

$$\mathbb{P}(\bar{T}) \leq (1+c) \exp(-d/8\sigma^2) + 2 \exp\left(-\frac{\|\boldsymbol{\mu}\|N}{2\sigma}\right) \quad (190)$$

Further, we can bound the probability $\mathbb{P}(T)$:

$$\mathbb{P}(\bar{T}) \leq (1+c) \exp(-d/8\sigma^2) + 2 \exp\left(-\frac{\|\boldsymbol{\mu}\|N}{2\sigma}\right) \quad (191)$$

$$1 - \mathbb{P}(T) \leq (1+c) \exp(-d/8\sigma^2) + 2 \exp\left(-\frac{\|\boldsymbol{\mu}\|N}{2\sigma}\right) \quad (192)$$

$$\mathbb{P}(T) \geq 1 - (1+c) \exp(-d/8\sigma^2) - 2 \exp\left(-\frac{\|\boldsymbol{\mu}\|N}{2\sigma}\right) \quad (193)$$

Therefore, the probability of the assumptions in Equations (184), (185), and (186) occurring simultaneously is at least $1 - (1 + c) \exp(-d/8\sigma^2) - 2 \exp(-\frac{\|\mu\|N}{2\sigma})$.

By using the triangle inequality, Equation (147) and the Assumptions (184) and (185) they can bound $\|\theta\|_2^2$:

$$\|\theta\|_2^2 = \|\mu + \frac{1}{2}\eta + \frac{1}{2}\omega\|_2^2 \quad (194)$$

$$\|\theta\|_2^2 \leq \|\mu\|_2^2 + \|\frac{1}{2}\eta\|_2^2 + \|\frac{1}{2}\omega\|_2^2 \quad (195)$$

$$\|\theta\|_2^2 \leq \|\mu\|_2^2 + \frac{1}{4}\|\eta\|_2^2 + \frac{1}{4}\|\omega\|_2^2 \quad (196)$$

$$\|\theta\|_2^2 \leq \|\mu\|_2^2 + \frac{1}{2}\frac{\sigma^2}{N}(d + \frac{1}{\sigma}) \quad (197)$$

$$\|\theta\|_2^2 \leq \|\mu\|_2^2 + \frac{\sigma^2}{N}(d + \frac{1}{\sigma}) \quad (198)$$

The reverse triangle inequality is defined as

$$|x - y| \geq ||x| - |y|| \quad (199)$$

$$|x - (-y)| \geq ||x| - |y|| \quad (200)$$

Using the reverse triangle inequality, Equations (147), (183) and Assumption (186) we have that

$$|\mu^T \theta| = |\mu^T \mu + \frac{1}{2}\mu^T \eta + \frac{1}{2}\mu^T \omega| \quad (201)$$

$$|\mu^T \theta| \geq |\mu^T \mu| - |\frac{1}{2}\mu^T \eta| - |\frac{1}{2}\mu^T \omega| \quad (202)$$

$$|\mu^T \theta| \geq \|\mu\|_2^2 - \frac{1}{2}\sigma^{1/2}\|\mu\|^{3/2} - \frac{1}{2}\|\mu\|_2^2 - \frac{1}{2}\frac{\sigma^2\epsilon}{2} \quad (203)$$

$$|\mu^T \theta| \geq \frac{1}{2}\|\mu\|_2^2 - \frac{1}{2}\sigma^{1/2}\|\mu\|^{3/2} - \frac{1}{2}\frac{\sigma^2\epsilon}{2} \quad (204)$$

$$|\mu^T \theta| \geq \frac{1}{2}(\|\mu\|_2^2 - \sigma^{1/2}\|\mu\|^{3/2} - \frac{\sigma^2\epsilon}{2}) \quad (205)$$

They have assumed that the signal/noise ratio is large: $\frac{\|\mu\|}{\sigma} = r \gg 1$. Thus, we can drop the absolute value, because we assume that the term inside the $||$ is larger than zero:

$$|\mu^T \theta| \geq \frac{1}{2}(\|\mu\|_2^2 - \frac{1}{r}\|\mu\|^{1/2}\|\mu\|^{3/2} - \frac{\|\mu\|_2^2\epsilon}{2r^2}) \quad (206)$$

$$|\mu^T \theta| \geq (1 - \frac{1}{r} - \frac{\epsilon}{2r^2})\frac{1}{2}(\|\mu\|_2^2) \quad (207)$$

We have

$$(1 - \frac{1}{r} - \frac{\epsilon}{2r^2}) \geq 0 \quad (208)$$

if $r \geq 1.36602540378443 \dots$ and $\epsilon \leq 1$, and therefore

$$|\boldsymbol{\mu}^T \boldsymbol{\theta}| \geq \frac{1}{2} (\|\boldsymbol{\mu}\|_2^2 - \sigma^{1/2} \|\boldsymbol{\mu}\|^{3/2} - \frac{\sigma^2 \epsilon}{2}) \quad (209)$$

Because of Equation (198) and the fact that if $x \leq y$ and $\text{sgn}(x) = \text{sgn}(y)$ then $x^{-1} \geq y^{-1}$ we have

$$\frac{1}{\|\boldsymbol{\theta}\|} \geq \frac{1}{\sqrt{\|\boldsymbol{\mu}\|_2^2 + \frac{\sigma^2}{N} (d + \frac{1}{\sigma})}} \quad (210)$$

We can combine the Equations (209) and (210) to give a single bound:

$$\frac{|\boldsymbol{\mu}^T \boldsymbol{\theta}|}{\|\boldsymbol{\theta}\|} \geq \frac{\|\boldsymbol{\mu}\|_2^2 - \sigma^{1/2} \|\boldsymbol{\mu}\|^{3/2} - \frac{\sigma^2 \epsilon}{2}}{2\sqrt{\|\boldsymbol{\mu}\|_2^2 + \frac{\sigma^2}{N} (d + \frac{1}{\sigma})}} \quad (211)$$

we define $\boldsymbol{\theta}$ such that $\boldsymbol{\mu}^T \boldsymbol{\theta} > 0$ and thus

$$\frac{\boldsymbol{\mu}^T \boldsymbol{\theta}}{\|\boldsymbol{\theta}\|} \geq \frac{\|\boldsymbol{\mu}\|_2^2 - \sigma^{1/2} \|\boldsymbol{\mu}\|^{3/2} - \frac{\sigma^2 \epsilon}{2}}{2\sqrt{\|\boldsymbol{\mu}\|_2^2 + \frac{\sigma^2}{N} (d + \frac{1}{\sigma})}} \quad (212)$$

The false negative rate $\text{FNR}(\boldsymbol{\theta})$ and false positive rate $\text{FPR}(\boldsymbol{\theta})$ are

$$\text{FNR}(\boldsymbol{\theta}) = \int_{-\infty}^0 \mathcal{N}(x; \frac{\boldsymbol{\mu}^T \boldsymbol{\theta}}{\|\boldsymbol{\theta}\|}, \sigma^2) dx \quad (213)$$

$$\text{FPR}(\boldsymbol{\theta}) = \int_0^{\infty} \mathcal{N}(x; \frac{-\boldsymbol{\mu}^T \boldsymbol{\theta}}{\|\boldsymbol{\theta}\|}, \sigma^2) dx \quad (214)$$

As $\mathcal{N}(x; \mu, \sigma^2) = \mathcal{N}(-x; -\mu, \sigma^2)$, we have $\text{FNR}(\boldsymbol{\theta}) = \text{FPR}(\boldsymbol{\theta})$. From Equation (212) we can see that as ϵ decreases, the lower bound of $\frac{\boldsymbol{\mu}^T \boldsymbol{\theta}}{\|\boldsymbol{\theta}\|}$ will increase. Thus, the mean of the Gaussian distribution in Equation (213) will increase and therefore, the false negative rate will decrease, which shows the benefit of sampling with high boundary scores. This completes the extended proof adapted from (Ming et al., 2022).